Independent modes of ganglion cell translocation ensure correct lamination of the zebrafish retina

Jaroslav Icha,[1] Christiane Kunath,[1] Mauricio Rocha-Martins,[1,2] and Caren Norden[1]

[1]Max Planck Institute of Molecular Cell Biology and Genetics, 01307 Dresden, Germany
[2]Instituto de Biofísica Carlos Chagas Filho, 21941-902 Rio de Janeiro, Brazil

The arrangement of neurons into distinct layers is critical for neuronal connectivity and function. During development, most neurons move from their birthplace to the appropriate layer, where they polarize. However, kinetics and modes of many neuronal translocation events still await exploration. In this study, we investigate retinal ganglion cell (RGC) translocation across the embryonic zebrafish retina. After completing their translocation, RGCs establish the most basal retinal layer where they form the optic nerve. Using in toto light sheet microscopy, we show that somal translocation of RGCs is a fast and directed event. It depends on basal process attachment and stabilized microtubules. Interestingly, interference with somal translocation induces a switch to multipolar migration. This multipolar mode is less efficient but still leads to successful RGC layer formation. When both modes are inhibited though, RGCs fail to translocate and induce lamination defects. This indicates that correct RGC translocation is crucial for subsequent retinal lamination.

Introduction

A conserved feature of the central nervous system (CNS) is its stratified organization. The accurate localization of neuronal subtypes into layers is established during development and is critical for the timely connection among neurons. Stratified organization thus helps to ensure CNS functionality. Because many neurons are born in defined proliferative zones away from their final location, neuronal lamination relies on correct neuronal translocation. Neuronal movements are dynamic and often depend on the surrounding environment (Marín et al., 2010; Cooper, 2013). Therefore, they are best understood by time-lapse in toto imaging experiments (Driscoll and Danuser, 2015). Despite this, insights about neuronal migration have often been generated using fixed tissue or ex vivo culture (Cooper, 2013). This is because many established model systems for studying neuronal migration (e.g., cerebellar granule neurons of rodents) are not easily imaged in intact embryos. Even though in toto imaging of neuronal translocation has been achieved in mouse embryos (Yanagida et al., 2012), the applicability of this experimental setup is limited. Consequently, model systems that allow live imaging in intact developing embryos need to be explored. Findings there can then be used to understand neuronal translocation events in less accessible parts of the CNS.

The zebrafish (*Danio rerio*) is an ideal model system for live imaging approaches because of its small size and translucency at embryonic stages. Part of its CNS, the retina is located at the surface of the animal, which makes it suitable for studying neuronal translocation and lamination. The retina consists of stereotypical layers of five well-defined neuronal cell types (photoreceptors, horizontal, bipolar, amacrine, and ganglion cells) and one glial cell type (Cajal, 1972; Galli-Resta et al., 2008). Layers arise rapidly between 30 and 72 h postfertilization (hpf), which in principle can be covered by a single imaging experiment. However, it is important to choose the right microscope. Whereas confocal microscopy can induce phototoxicity-related artifacts during zebrafish development (Jemielita et al., 2012) and is usually performed at lower temporal resolution (Poggi et al., 2005; Chow et al., 2015), light sheet fluorescence microscopy (LSFM) allows fast, less phototoxic imaging (Huisken et al., 2004; Stelzer, 2015). Consequently, LSFM is an ideal tool to image neuronal layering in the zebrafish retina.

The first neuronal lamination event in the retina is the formation of the retinal ganglion cell (RGC) layer. RGCs are the first retinal neurons born in vertebrates (Sidman, 1961; Cajal, 1972; Nawrocki, 1985). Upon their apical birth, RGCs move basally, spanning the complete apico–basal axis toward the lens, where their axons later form the optic nerve. Although it is known that RGCs can translocate by moving their soma while keeping the attachment to both apical and basal sides of the epithelium (Cajal, 1972; Hinds and Hinds, 1974; Zolessi et al., 2006), we still lack a thorough analysis of their translocation kinetics and modes. Additionally, the cell biological mechanisms of somal translocation are unknown, despite the fact that this is a widespread mode of neuronal movement during retinal (Chow et al., 2015) and brain development (Nadarajah et al., 2001).

Supplemental Material can be found at:
/content/suppl/2016/10/17/jcb.201604095.DC1.html
/content/suppl/2016/10/24/jcb.201604095.DC2.html

Based on high-resolution imaging of single-cell behavior, we analyzed the kinetics of RGC translocation. We show that RGC somal translocation is an active, directionally persistent process. Speed and directional persistence of somal translocation depend on intact microtubules (MTs) and basal cellular attachment. Interference with somal translocation can result in a switch to a multipolar migratory mode, which was not previously reported for RGCs. This multipolar mode is less efficient but allows RGCs to reach their correct location. Complete inhibition of RGC movements, however, substantially perturbs lamination of other retinal layers.

Results

Rapid RGC translocation is followed by a period of fine positioning

To study the emergence of the RGC layer and the kinetics of RGC translocation, we labeled these cells using constructs containing the *ath5 (atonal bHLH transcription factor 7* [*atoh7*]*)* promoter (Fig. 1 A; Brown et al., 1998; Masai et al., 2003). Ath5 is expressed during the last cell cycle in a subset of apically dividing progenitor cells and produces one RGC and one cell that later gives rise to photoreceptors (Poggi et al., 2005; He et al., 2012). To label and follow RGCs between their apical birth and axonogenesis, we made use of previously published *Tg(ath5:gap-GFP/RFP)* lines (Zolessi et al., 2006), which express membrane-targeted GFP or RFP in the *ath5* lineage (Fig. 1, A and B). To achieve mosaic labeling and follow single RGCs, we injected *ath5* plasmid DNA into one-cell-stage embryos (for example, see Fig. S1, G–I).

We noted that the use of spinning disk microscopy even at low intensity illumination induced a slowing of RGC translocation compared with an LSFM setup (Fig. 1 C and Fig. S1 A). As the two microscope setups differ in the way the sample is mounted, we tested the influence of mounting and compared the viability and development of embryos mounted for LSFM or spinning disk microscopy to nonmounted embryos (Fig. S1 B). No change in heart rate or apoptosis was observed (Fig. S1, C–E). We thus concluded that the observed differences in RGC translocation speed are likely the result of higher phototoxicity induced by spinning disk microscopy. Thus, we used LSFM-generated data to analyze RGC translocation kinetics. No delay of RGC layer formation was observed in embryos imaged for 12–16 h compared with nonimaged controls.

Following emerging RGCs with live imaging (Video 1) revealed that RGC translocation could be divided into two parts that in total took ∼285 min (median; n = 50 cells and 19 experiments; Fig. 1, B and D). Initially, cells translocated basally for 115 min (median; n = 140 cells and 24 experiments) in a fast, persistent manner, moving ∼28 µm away from the apical side (median; n = 140 cells and 24 experiments; Fig. 1, B and D). Next, RGCs exhibited slower, more random movements within the RGC layer for 165 min (median; n = 50 cells and 19 experiments; Fig. 1 D and Fig. S1 F), moving on average 3 µm basally, which probably reflects growth of the retina rather than net cell movement. We termed this second phase of movement fine positioning. It ended with axonogenesis, which is the moment when a persistent growth cone emerged from the RGC. Only during fine positioning did cells lose their apical process, around 60 min before axonogenesis (median; n = 33 cells and 16 experiments), although the exact timing varied (Fig. S1 F).

To quantify the kinetics and directional persistence of the two phases of RGC movement, we calculated mean squared displacements (MSDs; Leung et al., 2011; Okamoto et al., 2013) from manually tracked 2D trajectories (Fig. 1 E). MSD analysis allows determination of the directionality of a particle (in this case, the nucleus) from the shape of the MSD curve. A linear curve indicates random motion, and a supralinear curve indicates directional motion. MSD analysis showed that the initial basal movement of RGCs was directionally persistent, as indicated by the α value of 1.60 ± 0.09 from fitting the MSDs with $2D_\Delta t^\alpha$ (see Materials and methods). In contrast, MSDs of cells undergoing fine positioning showed an almost linear relationship with time with the α value of 1.32 ± 0.09 (Fig. 1 E), indicating random motion. We also calculated the directionality ratio of the trajectories. Here, values close to 1 imply high directionality, and values approaching 0 imply random motion (Fig. 1 F). This analysisconfirmed that initial basal translocation is much more directed than fine positioning (Fig. 1 F). RGCs moved with a median instantaneous velocity of 0.26 µm/min in the directional phase and 0.02 µm/min during fine positioning (Fig. S1 A). We conclude that RGC translocation to the basal retina before RGC layer formation consists of a directional and a fine positioning phase.

Basal movement of RGC and progenitor nuclei is more efficient when cells inherit the basal process

Our analysis showed that initial RGC translocation is directionally persistent. Two scenarios could explain this directionality: (1) RGCs are displaced basally by the surrounding progenitor nuclei undergoing directed apical migration; or (2) RGC movements are driven cell autonomously and occur independently of movements within surrounding cells.

To test option 1, we stalled cells in S phase using a combination of aphidicolin and hydroxyurea (Fig. 1 G). Cell cycle inhibition started at 34 hpf, when the first pool of RGCs was born and co-inhabited the retina together with an abundant pool of progenitor cells (Kay et al., 2005). Apical migration of nuclei in these progenitor cells relies on progression through the cell cycle and was shown to be stalled in this condition (Leung et al., 2011). RGCs were either analyzed live (Fig. 1 H) or fixed at 48 hpf, when the RGC layer was fully formed in controls (Fig. 1 I). Inhibition of proliferation was confirmed by the lack of antiphosphorylated histone H3 staining in drug-treated embryos (Fig. 1 I). Migration of RGCs still occurred (Fig. 1 H), and although the eyes of treated embryos were overall smaller, the RGC layer still formed (Fig. 1 I), arguing that RGC translocation depended on cell-intrinsic processes.

Various active modes of neuronal displacement are driven by the concerted action of the centrosome and associated Golgi apparatus (Solecki et al., 2004; Bellion et al., 2005; Tsai et al., 2007). However, it was suggested that in RGCs, the centrosome remains in the apical process during translocation (Hinds and Hinds, 1974; Zolessi et al., 2006). To analyze how centrosomes and Golgis behave in RGC displacement, we used Centrin-tdTomato as a centrosomal marker and the trans-Golgi marker GalT-RFP. Live imaging showed that both structures remain in the apical process during somal translocation and only follow the nucleus toward more basal positions once the apical process is retracted in the fine positioning phase (Fig. S1, G and I; and Video 2). Similar observations were made for the primary cilium marked by Arl13b-mKate2 (Fig. S1 H and Video 2;
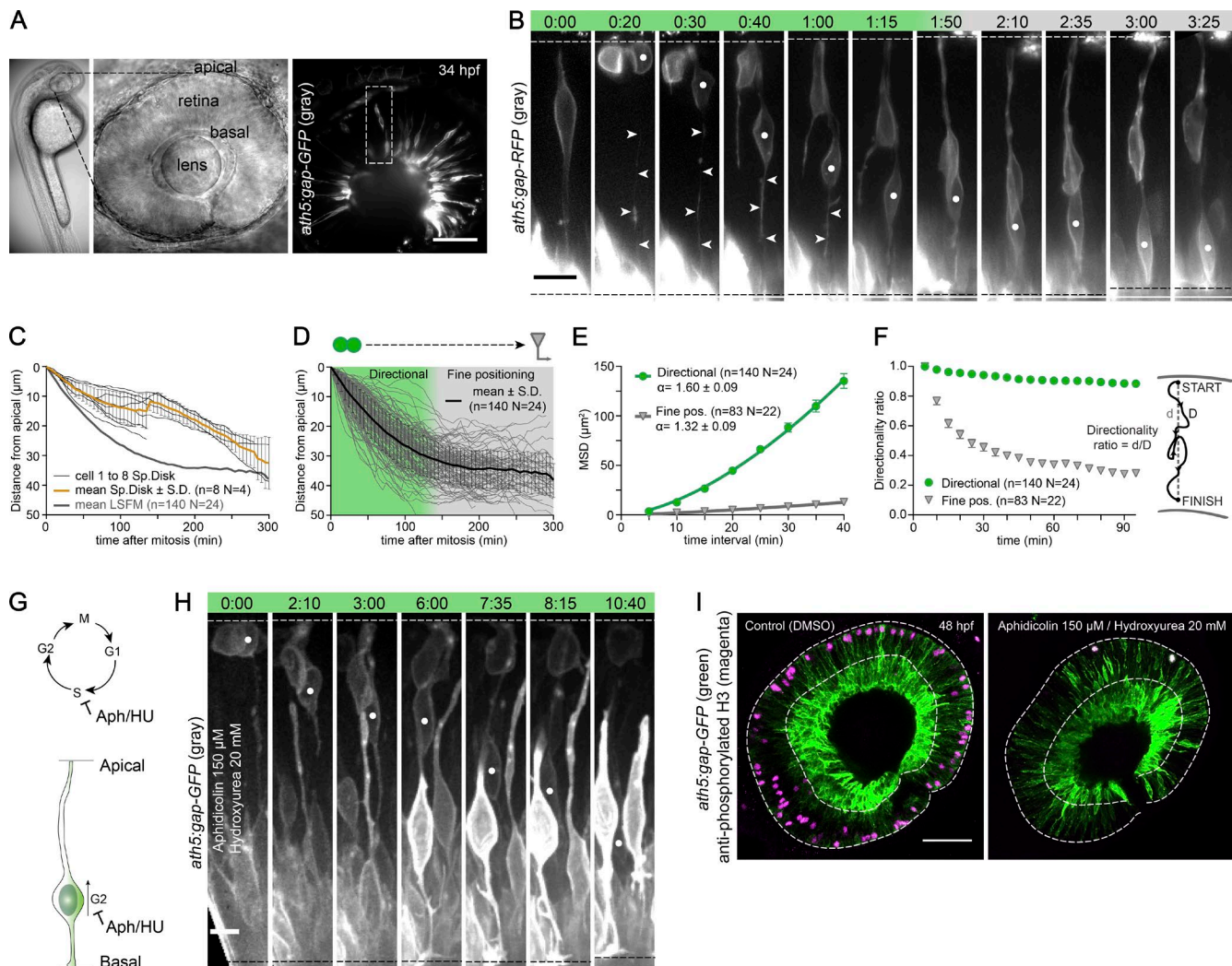
Figure 1. **RGC translocation kinetics.** (A) Developing eye of a 34-hpf embryo. *ath5:gap-GFP* transgene labels RGCs. The dashed box shows the typical area displayed in subsequent montages. Bar, 50 µm. (B) Typical example of RGC translocation in LSFM. Arrowheads, basal process. Bar, 10 µm. (C) Kinetics of RGC translocation in a spinning disk confocal microscope. 0 indicates mitotic position of cells. Eight single trajectories (*n* = 4 experiments) and a mean trajectory ± SD are shown plus the mean of wild-type trajectories in LSFM. (D) Kinetics of RGC translocation in LSFM. 0 indicates mitotic position of cells. 140 single trajectories and a mean trajectory ± SD are shown. Green phase, directionally persistent movement; gray phase, fine positioning. (E) MSDs of RGCs for directional phase and fine positioning. MSDs are from the first 95 min after mitosis and the first 95 min after reaching the basal side. α value is given with a 95% confidence interval. (F) Directionality ratio of RGCs in directional movement and fine positioning. Data from E. (E and F) Error bars represent SEM. Final directionality ratios: directional = 0.88; fine positioning = 0.28. The scheme defines the directionality ratio between the distance from start to finish of the trajectory (d) and the length of the trajectory (D). (G) Aphidicolin/hydroxyurea stalls cells in S phase. Thus, nuclei do not migrate toward the apical side for mitosis. (H) *ath5:gap-GFP* embryos treated with 150 µM aphidicolin/20 mM hydroxyurea imaged in a spinning disk microscope from 34 hpf. Imaging started 1 h after drug addition. Bar, 5 µm. (B and H) White dots, RGC followed. Time is shown in hours and minutes. Dashed lines delimit the apical and basal sides. (I) RGC layer still forms upon cell cycle inhibition. Fewer mitotic cells (right) compared with control (left) are seen by pH3 staining (magenta). Dashed lines mark the retinal outline and RGC layer. Bar, 50 µm.

Lepanto et al., 2016). This suggests that these organelles do not actively lead nucleokinesis in RGCs.

Given that RGC displacement was not triggered by movement within surrounding cells and not driven by a centrosome-based mechanism, we turned our attention to the basal process. In the mouse retina (Saito et al., 2003) and cerebral cortex (Okamoto et al., 2013), the inheritance of the basal process can streamline basal displacement of progenitor cell nuclei. We thus investigated how basal process inheritance correlates with RGC displacement kinetics. Interestingly, the basal process was inherited preferentially by 78% of the RGCs (*n* = 109/140 cells). In the remaining 22% of RGCs, cells regrew the basal process later during their translocation. Translocation kinetics

of RGCs that inherited the basal process were faster than for RGCs that regrew it (compare Fig. 1 B with Fig. 2 A; also see Video 1). As seen in representative trajectories (Fig. 2 B; more trajectories in Fig. S2, F and G), RGCs not inheriting the basal process (*n* = 31/140 cells) moved basally more slowly (Fig. 2, E and F). The higher directional persistence of RGCs inheriting the basal process was apparent from MSDs (Fig. 2 G and Fig. S2 A), directionality ratios (Fig. 2 J), and instantaneous velocity distributions (Fig. S2 C). Even though the cells not inheriting the basal process took longer to reach basal positions (165 vs. 105 min, median; Fig. S2 E), the time interval between their apical birth and axonogenesis was comparable to the timing in cells inheriting the process (Fig. S2, D and E).
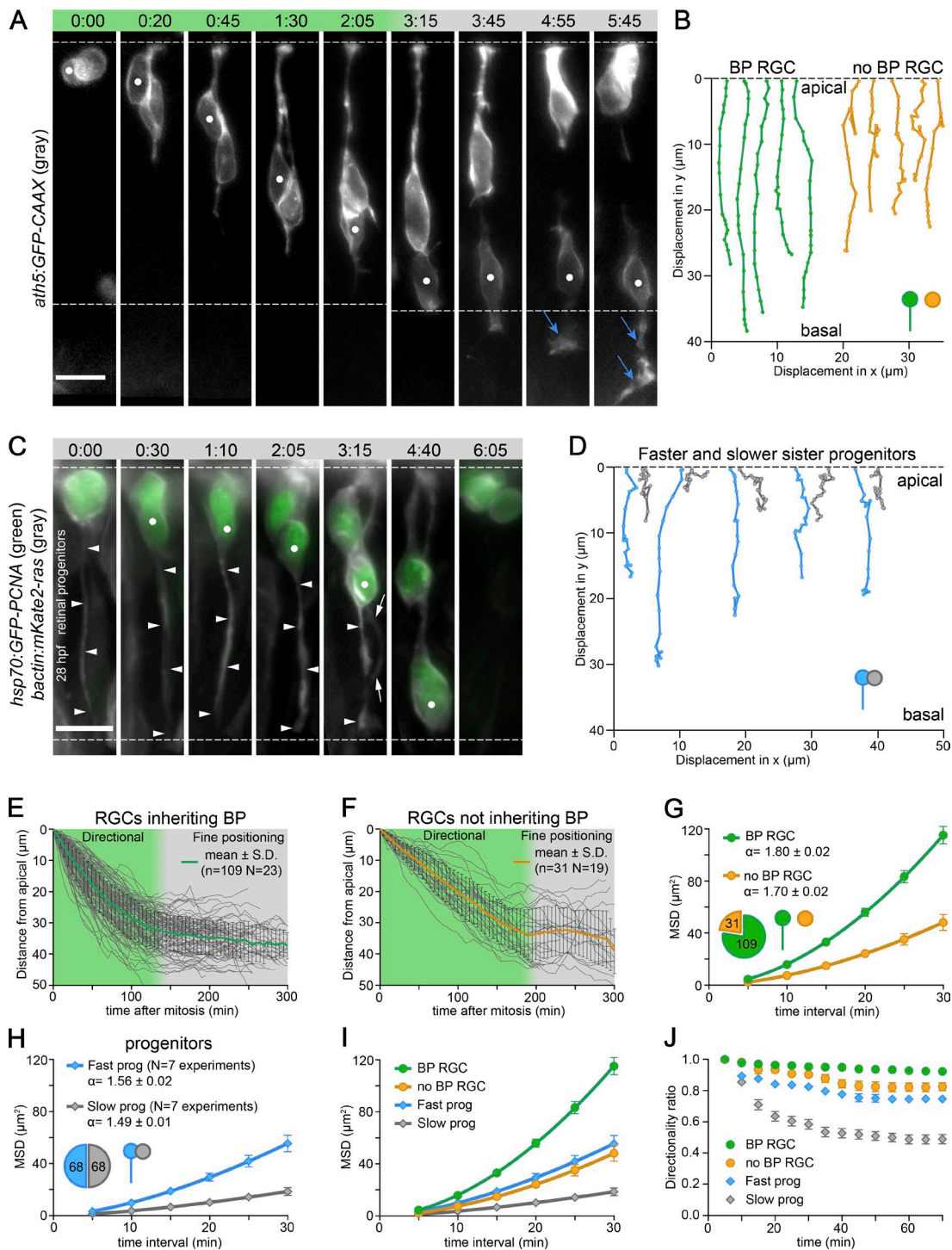
Figure 2. **Basal process inheritance streamlines basal nuclear translocation in RGCs and progenitors.** (A) Translocation of an RGC not inheriting the basal process (BP). Compare with Fig. 1 B. White dots, RGC followed; blue arrows, axon. Time is shown in hours and minutes. (B) Five representative 2D trajectories of RGCs inheriting (green) and RGCs not inheriting the basal process (BP; orange) for the first 95 min after cell division. More trajectories are in Fig. S2 (F and G). (C) Inheritance of basal process in progenitors. White dots, basal process inheriting progenitor; arrowheads, inherited basal process; arrows, newly formed basal process of sister cell. (A and C) Bars, 10 μm. (D) Five representative 2D trajectories of sister progenitors inheriting (blue) and not inheriting the basal process (gray) for the first 95 min after cell division. (E) Kinetics of RGC translocation with basal process. 0 indicates the mitotic position of cells. Single trajectories and a mean trajectory ± SD are shown. (F) Kinetics of RGC translocation without basal process. (E and F) Green phase, directionally persistent movement; gray phase, fine positioning. (G) MSDs of translocating RGCs with and without basal process. MSDs are calculated from the first 70 min after mitosis. (H) MSDs of faster and slower translocating sister progenitor nuclei. MSDs are calculated from the first 70 min after mitosis. (G and H) The α value is given with a 95% confidence interval. (I) Comparison of MSDs of RGC and progenitor nuclear translocation. Graph shows combined data from G and H. (J) Directionality ratios of RGC and progenitor nuclear translocation. The mean of all tracks is shown. Error bars represent SEM. Final directionality ratios: basal process RGC = 0.92, no basal process RGC = 0.82, fast progenitor = 0.75, slow progenitor = 0.49.

Retinal progenitors share many morphological similarities with RGCs. Thus, we hypothesized that a positive effect of basal process inheritance on basal nuclear displacement also exists after apical progenitor divisions. Although it was reported that basal displacement of retinal progenitor nuclei fits the characteristics of a random walk (Norden et al., 2009; Leung et al., 2011), these analyses did not discriminate between progenitors with or without a basal process. To test whether progenitors show different kinetics of basal nuclear translocation depending on basal process inheritance, we analyzed them by labeling nuclei with proliferating cell nuclear antigen (PCNA)–GFP and membranes with mKate2-ras (Fig. 2 C and Video 1). The trajectories of the sister nuclei (n = 68 pairs and 7) moving away from the apical side differed in all instances followed (see examples in Fig. 2 D). One of the nuclei consistently showed higher directional persistence (Fig. 2 H and Fig. S2 B), directionality ratio (Fig. 2 J), and instantaneous velocity distributions (Fig. S2 C). In almost all (16/17) cases in which we confidently assigned basal process inheritance to one of the progenitors, the faster and more directionally persistent nucleus belonged to this progenitor cell. Nevertheless, in comparison to RGCs, the movement of nuclei in progenitors was slower and less directional (Fig. 2, I and J; and Fig. S2, A–C). Overall, these data indicate that basal process inheritance is an important factor for efficient basal nuclear translocation in RGCs as well as in progenitors. The fact that nuclear displacement in progenitors is slower than RGC displacement suggests that RGC translocation involves additional components.

Interference with basal process attachment impairs basal RGC movement

As basal process inheritance streamlined basal RGC movement, we tested how interference with basal process attachment to the basal lamina affects RGC translocation. We initially interfered with the basal lamina itself. A core component of the basal lamina is Laminin α1 (Fig. S3 A; Randlett et al., 2011b). Knockdown of *laminin α1* using a published morpholino (Randlett et al., 2011b) depleted Laminin from the basal retinal membrane (Fig. S3 B), and RGCs in this condition lost their basal process, leading to defective translocation and little net basal movement (Fig. S3 C). However, as Laminin depletion has diverse effects on late retinal formation (Fig. S3 B; Randlett et al., 2011b), we additionally interfered with basal RGC attachment by targeting the basal actin pool associated with focal adhesions and cellular attachment to the basal lamina (Martinez-Morales et al., 2009; Randlett et al., 2011a). We used the Arp2/3 complex inhibitor CK-666 (Nolen et al., 2009) and the Rho kinase (ROCK) inhibitor Rockout. Arp2/3 loss has recently been shown to disrupt basal attachment of radial glia cells in the mouse cerebral cortex (Wang et al., 2016). We determined the necessary inhibitor concentrations at which the basal actin was reduced while actin associated with apical adherens junctions was still present (Fig. S3, D and E). Apical staining in corneal cells revealed that Rockout treatment did not show major effects on cortical actin and microridges (Lam et al., 2015), whereas CK-666 treatment led to a disarray of microridges and apical area reduction (Fig. S3 F). However, both treatments led to basal process detachment (Fig. 3 A and see Fig. 5 F), and RGCs did not stably reattach their basal process after their final apical division and did not persistently move basally (Fig. 3 A and see Fig. 5 F and Video 3).

To investigate the long-term effects of these inhibitors on RGC displacement, we stained differentiated RGCs with a Zn5
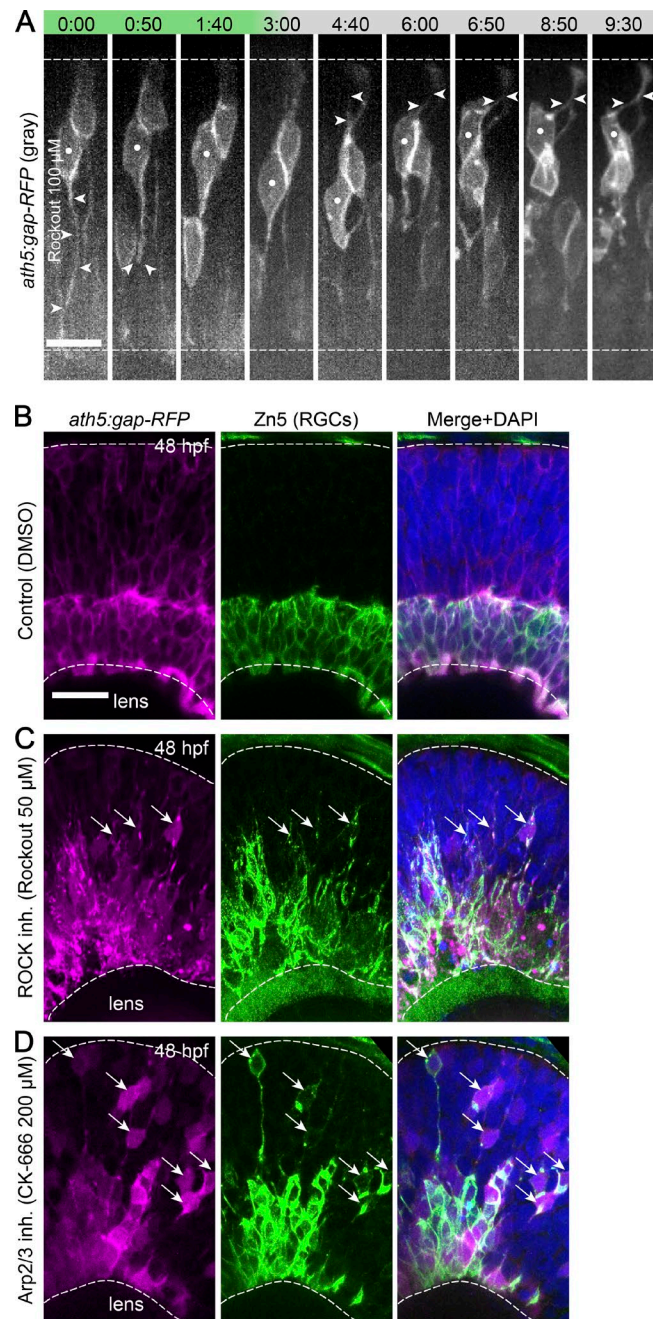
Figure 3. **Basal process attachment is important for RGC translocation.** (A) RGC translocation after ROCK inhibition. *ath5:gap-RFP* fish were imaged in a spinning disk microscope from 34 hpf. 100 μM Rockout was added at the start of imaging. White dots, RGC followed; arrowheads, basal and apical process. Time is shown in hours and minutes. Bar, 10 μm. (B) Zn5 staining for differentiated RGCs in control retina at 48 hpf. (C) Zn5 staining for differentiated RGCs after ROCK inhibition. (D) Zn5 staining for differentiated RGCs after Arp2/3 inhibition. (B–D) Arrows, ectopic RGCs. Dashed lines represent apical and basal sides. Bar, 20 μm.

antibody (Trevarrow et al., 1990) at 48 hpf, 16 h after drug addition. In both conditions, ectopic RGCs were observed in the middle of the retina, whereas in control retinas, Zn5-positive RGCs had formed a compact basal layer (Fig. 3, B–D). This means that cells differentiated into RGCs in time, even when they did not reach the most basal retinal layer. To substantiate our findings in the drug conditions and exclude pleiotropic

effects, we used a genetic approach. We overexpressed a C-terminal domain of the Arp2/3 complex activator N-WASP (NWASP-CA). This truncated protein binds but does not activate the Arp2/3 complex and thus acts as dominant negative for Arp2/3 activity (Rohatgi et al., 1999), similar to the CK-666 drug. Also, this approach affected the actin cytoskeleton (Fig. S3 F) and led to RGC translocation defects (see Fig. 5, G–J; and Fig. S4, H and I, discussed later), confirming that the specific disruption of basal process attachment indeed leads to impaired RGC translocation.

Efficient RGC movement depends on a stabilized MT cytoskeleton

As we observed that basal displacement is more efficient for RGCs than for progenitor cells (Fig. 2, H and I), we asked which other components play a role in nuclear translocation of RGCs. An attractive candidate was the MT cytoskeleton, which is involved in many modes of neuronal translocation (Solecki et al., 2004; Umeshima et al., 2007; Cooper, 2013). To test how MTs behave during RGC translocation, we first compared their growth dynamics in RGCs and progenitors using the plus tip marker end-binding protein 3 (EB3) (Fig. 4 A; Stepanova et al., 2003). EB3 labels the plus tips of MTs, called "comets," which allows for the measurement of MT growth rate. In both progenitors and RGCs, the majority of EB3 comets emanated from the apical centrosome and moved basally as shown previously (Fig. 4 A; Tsai et al., 2007; Norden et al., 2009). Notably, MT growth was faster in progenitors (0.23 vs. 0.13 µm/s; median; Fig. 4 A), demonstrating the difference in the MT dynamics between these two cell types. The slower comet speed in the RGCs was indicative of a more stabilized, less dynamic MT cytoskeleton. To test this idea, we stained embryos for acetylated tubulin as a readout of MT stabilization (LeDizet and Piperno, 1986). Additionally, all MTs were labeled with Doublecortin *Tg(bactin:GFP-DCX)* (Distel et al., 2010), an MT-associated protein. We further found that apical processes of translocating RGCs were, unlike progenitors, rich in acetylated tubulin (Fig. 4, F and G), corroborating the observation of slower EB3 comets in RGCs. To understand the emergence of the stabilized MTs, we examined them live in RGCs using *ath5* promoter-driven Doublecortin *ath5 :GFP-DCX*. MTs became enriched in the apical process shortly after cell division and remained there during the whole translocation (Fig. 4 B and Video 4).

We thus asked whether these apical MTs are important for RGC displacement using the MT depolymerizing drug colcemid. The drug was added at 32 hpf, and Zn5 antibody staining was performed 16 h later. This revealed that many RGCs were retained at midretinal positions (Fig. 4 D), whereas RGCs in controls formed a compact basal layer (Fig. 4 C), suggesting that MT depolymerization indeed interferes with RGC movement. To confirm this finding and interfere with MT stability in single cells in vivo, we generated a construct to overexpress the MT-destabilizing protein Stathmin 1 (Jourdain et al., 1997) under the control of a heat shock promoter (*hsp70*) for temporal control. Stathmin overexpression indeed led to MT depolymerization in the *Tg(bactin:GFP-DCX)* line (Fig. S4 A). Embryos were injected with an *hsp70:Stathmin1 -mKate2* plasmid, heat shocked at 24 hpf (to observe progenitor behavior) or 30 hpf (to observe RGC behavior), and imaged starting 4 h after heat shock. Stathmin overexpression had no effect on progenitor cell behavior, morphology, or interkinetic nuclear migration (Fig. S4 D). In contrast, RGCs lost their basal process after apical division (while keeping the apical process; Fig. 5 B, from 1:45 time point), initially leading to compromised movement (Fig. 4 E). In many cases, movement of RGCs was less directional than in the control situation, as initial basal movement was often followed by apical movement so that cell net displacement was marginal (Fig. S4, E and F, before apical process loss).

These data show that progenitors and RGCs differ in their MT arrangements. RGCs contain stabilized MTs in the apical process when translocating basally, and the stabilized MTs aid efficient RGC displacement.

RGCs can switch to a multipolar migratory mode upon disturbance of MTs or Arp2/3 inhibition

Stabilized MTs in the apical process and maintenance of the attachment of the basal process to the ECM are important factors for efficient RGC translocation. However, in both conditions, we noted that, although some cells were observed at ectopic locations, many RGCs still reached the basal side (Fig. 3, C and D; and Fig. 4 D). We thus asked how and when RGC movement took place when basal process attachment or the MT cytoskeleton was compromised. In the control scenario, RGCs were observed to lose their basal process in very rare cases. These cells subsequently detached their apical process, increased their protrusive activity, and moved basally in a multipolar migratory mode (Fig. 5 A and Video 5). To test whether a comparable switch to multipolar migration takes place in RGCs upon interference with MT stability, we imaged Stathmin-overexpressing cells for 12–16 h. In this experiment, Stathmin overexpression led to depletion of acetylated MTs (Fig. S4 B). As noted before, cells initially kept their apical process and did not generate much net movement toward basal positions (Fig. 4 E). Upon continued Stathmin expression, however, cells lost their apical attachment ~200 min after apical division (*n* = 20 and 5; median). After that point, these cells switched to a multipolar migratory mode (Fig. 5, B and C; and Video 5), as seen for the rare control examples. Multipolar cells lost polarity, as shown by random positioning of the MT-organizing center (Fig. S4 C). Once multipolar migration started, instantaneous velocities increased (Fig. S4, E and F). Multipolar migration was directionally persistent, as shown by supralinear MSDs with an α value of 1.53 ± 0.03 (Fig. 5 D). However, it was not as efficient as somal translocation of RGCs inheriting the basal process (Fig. 5 D), as seen in the directionality ratio (Fig. 5 E). Similar observations were made upon Arp2/3 inhibition by CK-666 (Fig. 5 F). Upon drug treatment, RGCs first lost their basal process and later their apical process and translocated via the multipolar mode (Fig. 5 F). Also, after overexpressing NWASP-CA, RGCs fell into the multipolar mode to reach basal positions (Fig. 5 G, *n* = 18 and 4; and Video 5), whereas this condition had no effect on progenitors (Fig. S4 G). The movement of RGCs after Arp2/3 inhibition was not as directed as in the Stathmin condition (Fig. 5, H–J; and Fig. S4, H and I). This could indicate that Arp2/3 activity is also involved in driving this migratory mode and not only in basal process attachment.

Multipolar movement was seen previously for amacrine cells (ACs; Chow et al., 2015). Therefore, we imaged translocating ACs to compare their behavior with that of RGCs. ACs
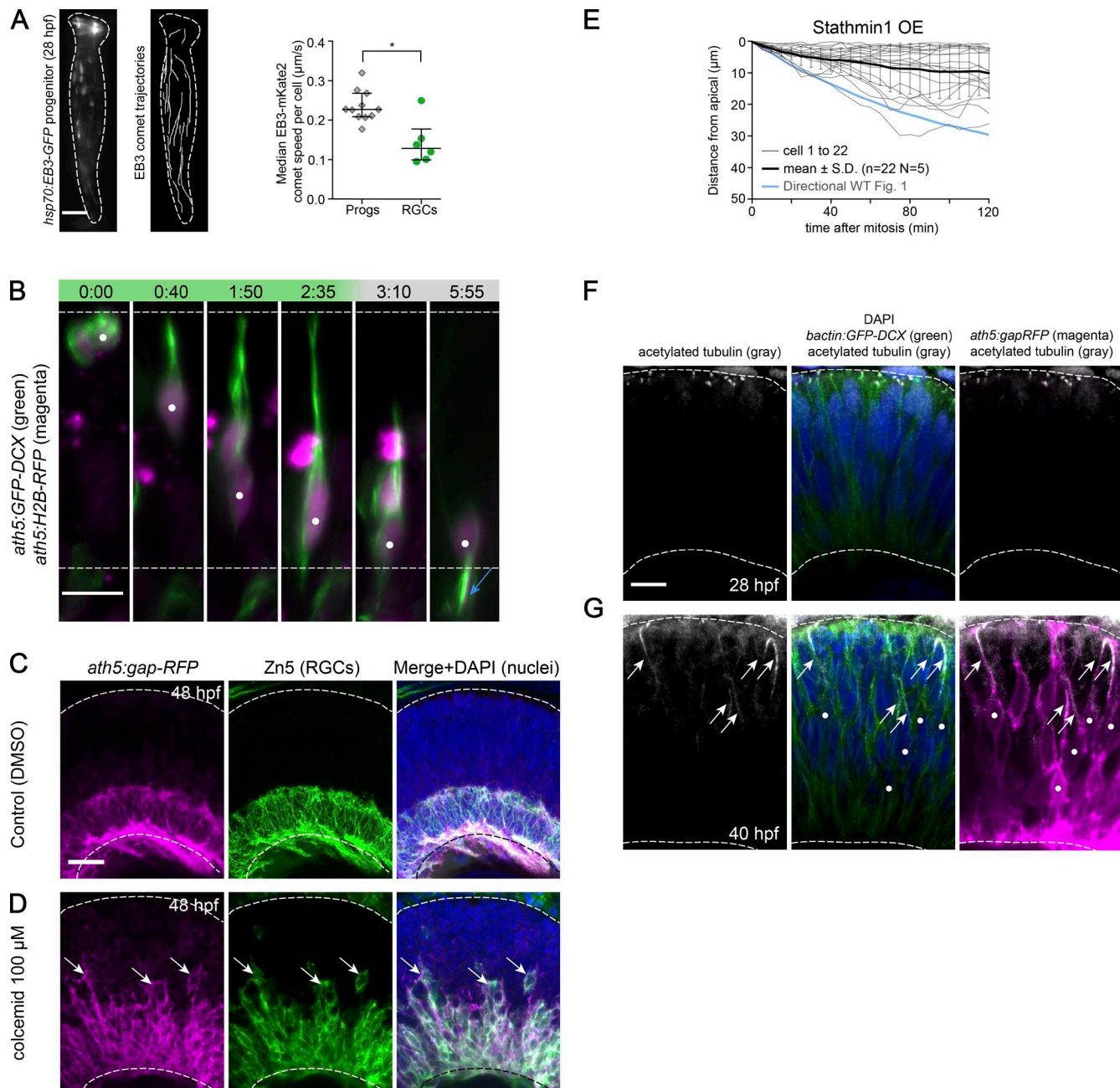
Figure 4. Stabilized MTs are important for RGC translocation. (A, left) Example of EB3 comets in progenitor cells. Bar, 5 µm. (Right) Progenitor EB3 comet speed median = 0.23 µm/s; n = 11 cells, 60 comets. RGC EB3 comet speed median = 0.13 µm/s; n = 6 cells, 24 comets; *, P = 0.0103, Mann-Whitney U test. Bars represent median and interquartile ranges. (B) Live imaging of MTs in translocating RGCs. Time is shown in hours and minutes. White dots, RGC followed; blue arrow, axon. Bar, 10 µm. (C) Staining for differentiated RGCs with Zn5 antibody in control retina at 48 hpf. (D) Zn5 staining in retinas treated with colcemid. (E) MT destabilization by overexpression (OE) of Stathmin 1 (*hsp70:Stathmin1-mKate2*) stalls RGC translocation. Heat shock applied at 30 hpf, imaging from 34 hpf. Graph shows all trajectories after RGC terminal division, the mean trajectory ± SD, and the mean trajectory in the wild-type situation. (F) Acetylated tubulin staining in progenitors. MTs were labeled by *bactin:GFP-DCX*. At 28 hpf, only apical primary cilia in progenitors are stained. Bar, 10 µm. (G) Acetylated tubulin staining in RGCs. All MTs were labeled by *bactin:GFP-DCX*. At 40 hpf, acetylated tubulin is seen in the apical process of RGCs (white arrows). White dots, translocating RGCs. (C, D, F, and G) Dashed lines represent apical and basal sides. Arrows, ectopic RGCs. Bar, 20 µm.

also initially showed a bipolar morphology and moved only slowly toward the inner nuclear layer (Fig. S4 J). However, once these cells lost their apical process attachment, their velocities and directionality increased (Fig. S4, K–M; and Video 5) similarly to RGCs. These results indicate that RGC migration is a robust process and cells can adopt an alternative, although less efficient, multipolar mode of movement.

Complete arrest of RGC translocation and their ectopic maturation disturbs retinal lamination

The surprising finding that RGC translocation can occur via a multipolar migratory mode argued that RGC movement is particularly robust. We speculated that this robustness exists because a failure of RGC displacement would have severe
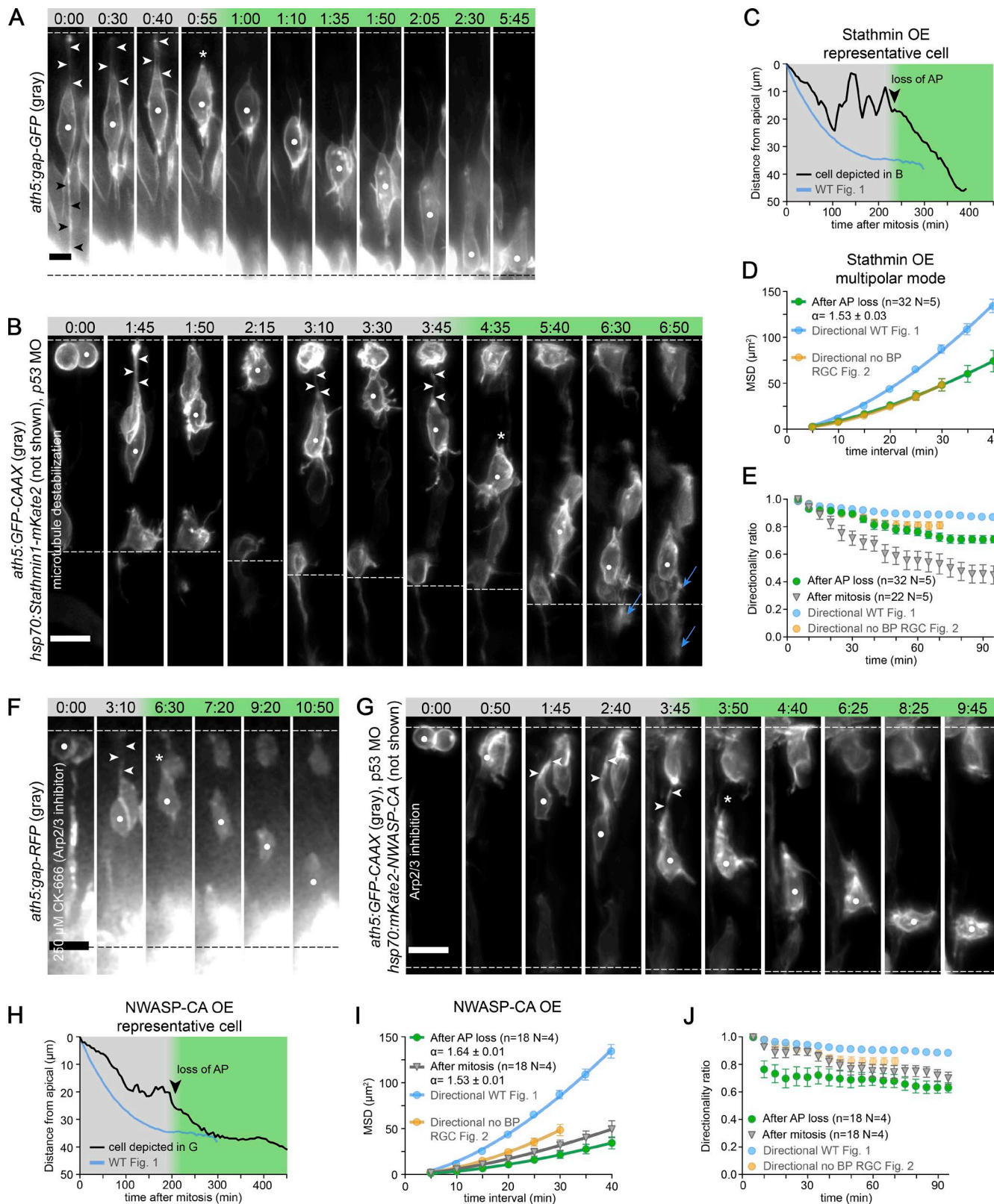
Figure 5. **RGCs can switch to a multipolar migratory mode.** (A) Rare example of multipolar migration in control embryos. Bar, 5 µm. (B) Multipolar migration induced by MT destabilization. Stathmin 1 overexpression induced at 30 hpf. Time lapse starts at 34 hpf. (A and B) Gray phase, cell still has the basal and apical process (A) or apical process (B); green phase, directional multipolar mode; white dots, RGC followed; arrowheads, apical and basal process (A) or apical process (B); asterisks, apical process loss; blue arrows, axon. Bar, 10 µm. (C) Typical trajectory of RGCs with destabilized MTs from the montage in B. Arrowheads, loss of the apical process (AP). More trajectories are in Fig. S4 E. The mean wild-type (WT) trajectory is shown. (D) MSDs of RGCs in multipolar migratory mode. Values are taken from the first 95 min after apical process loss. Wild type from Fig. 1 E and RGCs without basal process from Fig. 2 G. The α value is given with a 95% confidence interval. (E) Directionality ratios before and after apical process loss. Values are taken

consequences for retinal development. To test this, we needed a condition in which both displacement modes were impaired. It was previously shown that overexpression of a membrane-targeted atypical PKC-ζ (aPKC-CAAX) restructures actin cytoskeleton in progenitor cells (Strzyz et al., 2015). Therefore, we tested whether overexpression of this construct could suffice to block RGC basal process attachment but allow cells to keep their apical process. Phalloidin staining of the apical surface of corneal cells in the *Tg(hsp70:mKate2-aPKC-CAAX)* line revealed disorganized and less abundant microridges but increased cortical actin (Fig. S3 F). This transgenic line was thus imaged in combination with a *Tg(ath5:gap-GFP)* line. Heat shock was performed between 30 and 32 hpf so that aPKC-CAAX was present when RGC emergence was at its peak. Subsequently, RGCs lost their basal process after apical division but for >6 h kept their apical process (whereas the apical process was lost after 200 min [median] in the Stathmin condition). This resulted in RGCs arrested at apical and central retinal regions (Fig. 6 A and Video 6) and projecting axons from there. The analogous phenotype was observed when aPKC-CAAX expression was restricted to the *ath5* lineage using *ath5:mKate2-aPKC-CAAX* (Fig. 6 D and Video 6). Results from live imaging were confirmed by Zn5 staining, which also showed ectopic RGCs in midretinal regions (Fig. 6, B and C; and Fig. S5 B).

To assess whether this impairment of RGC translocation had long-lasting effects on retinal lamination, we imaged *Tg(hsp70:mKate2-aPKC-CAAX)* fish crossed with the *SoFa2* line (Almeida et al., 2014), which labels membranes of all retinal cells using a combination of three fluorescent proteins. Fish were imaged by LSFM every 12 h between 36 and 84 hpf to follow retinal lamination (Fig. 6 E). Control *SoFa2* retinas showed normal lamination (Fig. S5 A), whereas in combination with the *Tg(hsp70:mKate2-aPKC-CAAX)* line heat shocked at 32 hpf, RGCs were misplaced, and this displacement was not corrected over development (Fig. 6 E, arrows). Notably, the formation of other neuronal layers was also perturbed, with neurons aberrantly positioned and, in some cases, arranging around ectopically placed RGCs. This misplaced layering persisted until 96 hpf, and bipolar cells could sometimes be seen wrapped around ectopic RGC patches (Fig. 7 B). Milder lamination defects also occurred after mosaic expression of *ath5:mKate2-aPKC-CAAX* from injected DNA (Fig. 7 C).

We needed to ensure that the observed phenotypes in the *Tg(hsp70:mKate2-aPKC-CAAX)* line did not originate from defects in later translocation or neurogenesis events but were caused specifically by RGCs, which failed to translocate. To this end, we compared embryos heat shocked at different developmental stages. We overexpressed aPKC-CAAX at the peak of RGC generation, after the peak, and when the RGC

layer was fully formed, i.e., at 30, 36, and 48 hpf. Imaging at 96 hpf confirmed the severe lamination defect in the fish heat shocked at 30 hpf (Fig. S5 C). In contrast, fish heat shocked at 36 hpf showed only a few ectopic cell clusters (Fig. S5 D, arrowheads), and fish heat shocked at 48 hpf (Fig. S5 E) were indistinguishable from controls (Fig. 7 A). Additionally, we used a published *ath5* morpholino (Pittman et al., 2008), as the absence of Ath5 is known to suppress RGC generation (Kay et al., 2001). This enabled us to test whether lamination defects also occurred when no RGCs were present. *Tg(hsp70:mKate2-aPKC-CAAX, ath5:gap-RFP, vsx1:GFP)* embryos injected with *ath5* morpholino heat shocked at 30 hpf showed an RGC layer partially filled with bipolar cells and no optic nerve (Fig. 7 D; Kay et al., 2001). The otherwise normal lamination (Fig. 7 D) of their retina at 96 hpf in all examined embryos strongly argued that defects seen in the *Tg(hsp70:mKate2-aPKC-CAAX)* fish were caused by the ectopically differentiating RGCs. Thus, successful RGC basal translocation is crucial for later retinal lamination.

Discussion

In this study, we investigate the first step of neuronal lamination in the retina, the formation of the RGC layer. We reveal the kinetics of RGC somal translocation and show that it represents a directed movement dependent on basal process attachment and MTs. When RGC somal translocation is impaired, cells can resort to multipolar migration. When both modes are inhibited, RGCs fail to translocate, and the resulting misplaced RGCs induce lamination defects, indicating that RGC translocation represents a crucial first step for the formation of other retinal layers. We summarize our main findings in Fig. 8.

Parallels between emerging RGCs and retinal progenitors

RGCs are the first neurons born in the vertebrate retina (Sidman, 1961; Cajal, 1972; Nawrocki, 1985), when most of the retinal cells are still apically dividing neuroepithelial progenitors. At first sight, apical progenitors and emerging RGCs appear similar: they both display neuroepithelial traits, and the nucleus represents the bulkiest part of the cell. In addition, both cell types translocate their nuclei toward basal positions more efficiently when they inherit the basal process. However, basal nuclear displacement is faster in RGCs, arguing that additional mechanisms are present in these cells. Notably, the two cell types also differ in the organization of their MT cytoskeleton: in progenitor cells, MTs are more dynamic, whereas RGCs feature stabilized MTs, which are involved in efficient basal translocation of their soma.

---

from the first 95 min after mitosis and the first 95 min after apical process loss. Final directionality ratios: after apical process (AP) loss, 0.71; after mitosis, 0.45. Wild type from Fig. 1 F and RGCs without basal process (BP) from Fig. 2 J. (F) Multipolar migration induced by Arp2/3 inhibition. *ath5:gap-RFP* fish were imaged in a spinning disk microscope from 34 hpf. CK-666 was added at the start of imaging. Images were denoised in Fiji (ROF denoise). (G) Multipolar migration induced by Arp2/3 inhibition. NWASP-CA overexpression was induced at 30 hpf. Time lapse starts at 34 hpf. (F and G) Gray phase, cell has apical process; green phase, directional multipolar mode; white dots, RGC followed; arrowheads, apical process; asterisks, apical process loss. Dashed lines delimit the apical and basal sides. Bars, 10 μm. (H) Typical trajectory of RGCs upon NWASP-CA overexpression (OE) from the montage in G. Arrowhead, apical process loss. More trajectories are in Fig. S4 H. The mean wild-type trajectory is shown. (I) MSDs of RGCs after Arp2/3 inhibition (NWASP-CA overexpression). Wild type from Fig. 1 E and RGCs without basal process from Fig. 2 G. The α value is given with a 95% confidence interval. (J) Directionality ratios of RGCs after mitosis and after apical process loss upon NWASP-CA overexpression. (I and J) Values are taken from the first 95 min after mitosis and the first 95 min after apical process loss. Error bars represent SEM. Final directionality ratios: after apical process loss = 0.63; after mitosis = 0.70. Wild type from Fig. 1 F and RGCs without BP from Fig. 2 J.
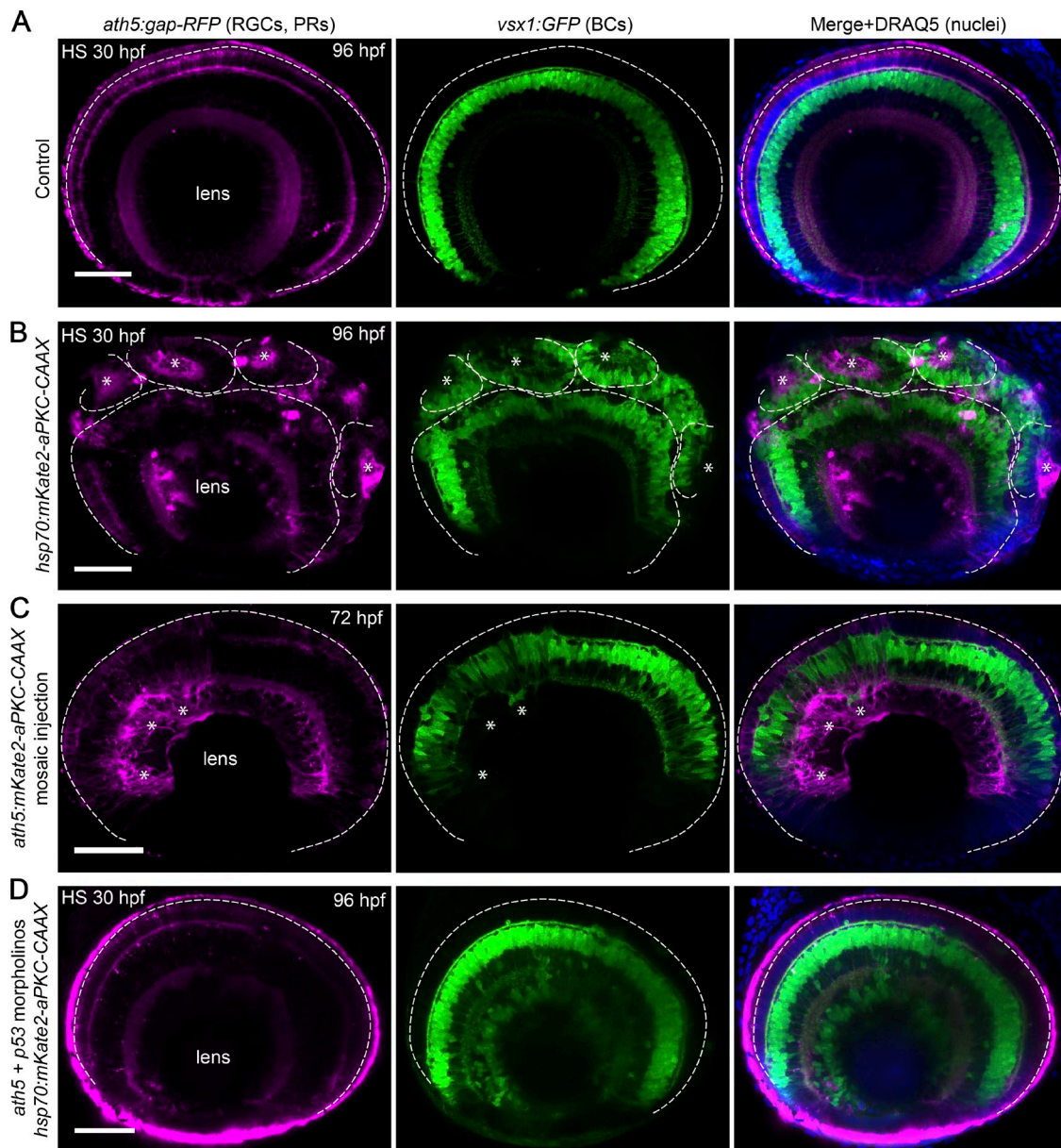
Figure 6. **RGC translocation is stalled upon aPKC-CAAX overexpression and is not rescued over time.** (A) No RGC translocation upon aPKC-CAAX overexpression. (B) Zn5 staining for differentiated RGCs in control retina at 48 hpf. Bar, 20 µm. (C) Zn5 staining of aPKC-CAAX–overexpressing retina at 48 hpf. (B and C) Dashed lines delimit apical and basal sides. (D) aPKC-CAAX expression specifically in the *ath5* lineage stops RGC translocation and leads to ectopic polarization. (A and D) White dots, RGC followed; arrowheads, apical process; asterisk, loss of apical process; blue arrows, axon. Time is shown in hours and minutes. Bars, 10 µm. (E) The *SoFa2* transgenic fish (combination of *ath5:gap-RFP* [labeling RGCs and photoreceptors (PRs)], *crx:gap-CFP* [labeling photoreceptors and bipolar cells (BCs)], and *ptf1a:Gal4-VP16 UAS:gap-YFP* [labeling horizontal cells (HCs) and ACs]) imaged every 12 h. Fish were kept in the incubator between time points. Ectopic RGCs developed at the temporal (T) side of retina. The nasal (N) side developed as a control (see Fig. S5 A). Arrowheads, clusters of RGCs that trigger ectopic lamination of other cell types; arrows, clusters of RGCs that interrupt the normal lamination without triggering ectopic layers; dashed boxes, magnified area. HS, heat shock; D, dorsal; V, ventral. Bars, 20 µm.

Figure 7. Ectopically differentiated RGCs induce retinal lamination defects. (A) Control retina at 96 hpf with RGCs, photoreceptors (PRs; magenta), and bipolar cells (BCs; green) labeled. Nuclei are stained with DRAQ5 (blue). HS, heat shock. (B) Organizing role of ectopic RGCs. Asterisks, clusters of ectopic RGCs organizing later-born bipolar cells. (C) Lamination defects after mosaic expression of *ath5:mKate2-aPKC-CAAX*. Asterisks, area with the lamination defect. (D) Retinal lamination upon aPKC-CAAX overexpression in the absence of RGCs. The *ath5:gap-RFP* reporter is still expressed in other cell types when RGCs are absent in the *ath5* morphant. No optic nerve is seen. (A–D) Dashed lines delimit the apical side or indepedent areas of lamination. Bars, 50 µm.

Cellular requirements for RGC somal translocation

The most efficient mode of RGC basal movement is somal translocation. Most RGCs inherit the basal process after their last apical division, which helps their efficient translocation. When basal process attachment is impaired, RGC translocation is less efficient, and cells often arrest and form their axons in midretinal positions. In addition to basal process attachment to the basal lamina, we show that MTs in the apical process are important for efficient basal translocation of RGCs. These stabilized MTs might prevent the nucleus from sliding back toward apical positions and allow the movement to be more persistent compared with progenitors.

It is possible that lateral interactions between RGCs and their neighboring progenitors (e.g., via contacts to their basal processes) play an inductive role in efficient somal translocation. Such observations have been made in other systems (Elias et al., 2007; Famulski et al., 2010; Marín et al., 2010), and it will be interesting to address whether and how neighboring cells influence RGC movements.

RGCs can switch to a multipolar mode when somal translocation is perturbed

Surprisingly, even when basal process attachment or stabilized MTs are disturbed, RGCs still can reach the basal RGC layer. In these scenarios, cells are stalled at the apical retina before
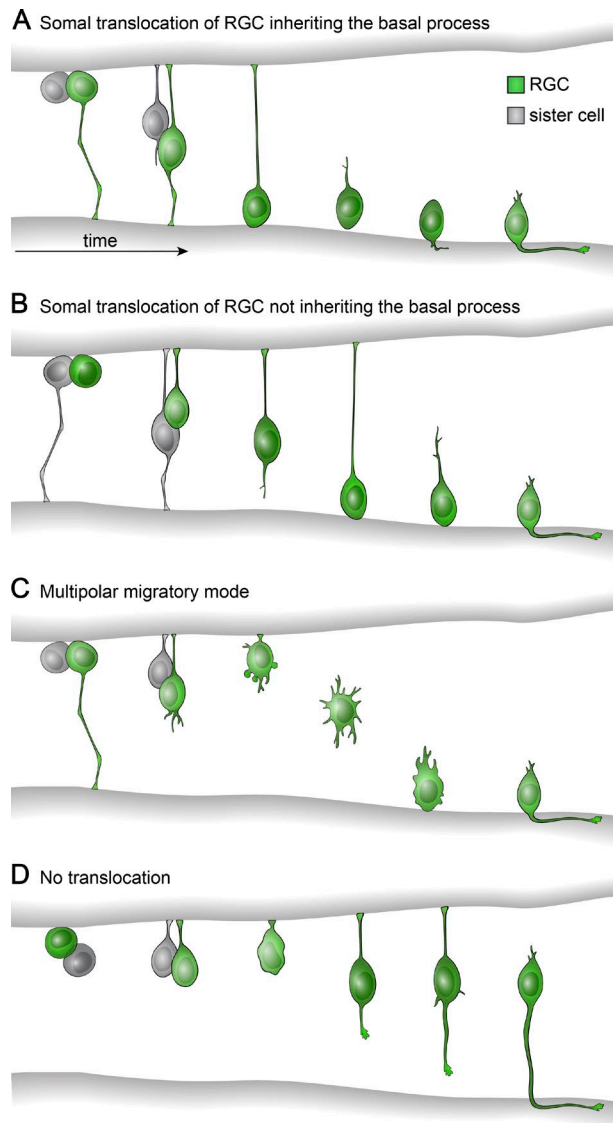
Figure 8. Scheme of different RGC translocation scenarios. (A) Somal translocation of RGC inheriting the basal process, a mode used by 80% of cells. The RGC translocates basally faster than the sister cell. Fine positioning, during which cells lose their apical processes and eventually form axons, follows. (B) Somal translocation of RGC not inheriting the basal process, a mode used by 20% of cells. The RGC initially lags behind the sister cell. Later, it regrows the basal process and overtakes it. Translocation is less efficient than in A. The fine positioning phase is shorter than in A. (C) The multipolar migratory mode occurs after MT destabilization or Arp2/3 inhibition and in rare cases in control cells. After loss of basal process attachment, the RGC detaches its apical process and increases protrusive activity. It then moves basally using the multipolar mode. This movement is less efficient than in A. Axon formation and RGC layer establishment are not affected. (D) No translocation. In case RGC translocation is inhibited, cells are able to differentiate at ectopic locations, which has severe consequences for later retinal lamination.

they retract their apical process and switch to a multipolar migratory mode. Once multipolar migration is initiated, it is only slightly less efficient than the directional phase of somal translocation. The reason for the preservation of RGC directional persistence could lie in the fact that, when RGCs emerge, the majority of the retina is still occupied by stably attached bipolar progenitors. These tightly packed, elongated progenitors might prevent tangential movement of RGCs. It is also possible that

additional guidance cues are involved in establishing the directionality of multipolar migration, and it will be interesting to explore these possibilities.

Notably, RGCs are not the only neuronal cell type capable of using two different translocation modes. It has been shown that projection neurons of the mouse cerebral cortex can use several different migratory modes, including somal translocation and multipolar migration (Tabata and Nakajima, 2003; Noctor et al., 2004). We further showed that ACs exhibit a similar pattern of a slower bipolar phase of translocation with the apical process and faster final multipolar movement after apical process loss. However, AC translocation is not directly affected by aPKC-CAAX overexpression, suggesting that the cascades driving apical detachment in ACs and RGCs are different. How apical detachment and the switch to multipolar migration differ between these two cell types will be an interesting question for future studies.

In conclusion, common patterns in neuronal migration in different organisms exist. This means that findings made in the zebrafish retina can be relevant for other areas of the developing CNS.

RGC layer formation orchestrates subsequent retinal lamination events

The finding that RGCs can switch their mode of movement reveals that RGC basal displacement is an unexpectedly robust process. We speculate that this robustness emerged to ensure later retinal lamination. When RGC translocation is compromised, all following lamination events are affected. Interestingly, we find that RGCs can organize later born cells around themselves when they are found at ectopic positions. It was shown that RGCs play an organizing role during inner plexiform layer formation (Kay et al., 2004), but it is also known that the zebrafish retina can laminate relatively normally when RGCs are absent (Kay et al., 2001). This is also seen in the combined aPKC-CAAX overexpression/*ath5* morphant condition in which retinal layering is normal, most likely because no ectopic RGCs are present. Overall, this suggests that even though RGCs are not required for retinal lamination per se, when they are present, they play an organizing role in later retinal development independent of their position.

Beyond the findings on RGC translocation and retinal lamination, this study exemplifies the importance of well-controlled in toto imaging for understanding the kinetics and mechanisms of CNS development. Using the gentlest microscopy available allowed us to generate a comprehensive dataset and study the process in question as close to the developmental "ground truth" as currently possible (Stelzer, 2015). If we had limited our study to comparing the "before" and "after" situation, many important insights would have been missed, including the multipolar migratory mode and the importance of basal process inheritance. Obviously, such experiments are not feasible in every tissue or model system. Still, we argue that studies like this will generate important advances in the understanding of CNS formation and reveal general principles that subsequently can be extended to other, less accessible systems.

Materials and methods

Zebrafish husbandry

Wild-type TL zebrafish were maintained and bred at 26°C. Embryos were raised in E3 medium at 28.5 or 32°C and treated with 0.2 mM

1-phenyl-2-thiourea (Sigma-Aldrich) from 8 to 10 hpf onward to delay pigmentation. Medium was changed daily. All animal work was performed in accordance with European Union directive 2011/63/EU as well as the German Animal Welfare Act.

Zebrafish transgenesis

1 nl Tol2 plasmid containing the ubiquitously expressed MT marker Doublecortin *Tg(bactin:GFP-DCX)* or *Tg(hsp70:mKate2-aPKC-CAAX)* at 30 ng/µl and Tol2 transposase RNA at 50 ng/µl in double-distilled H_2O supplemented with 0.05% phenol red (Sigma-Aldrich) was injected into the cytoplasm of one-cell-stage embryos. F_0 embryos with fluorescence signal were grown to adulthood, and Tg carriers were identified by outcross with wild-type fish.

Transgenic lines

See Table 1 for a list of transgenic lines.

Heat shock of embryos

To induce expression of the heat shock promoter (*hsp70*)–driven constructs, the Petri dish with embryos was placed into a water bath set to 37 or 39°C for 15–30 min. Imaging was started 3–4 h after heat shock.

Blastomere transplantations

Embryos at high to sphere stage were dechorionated in glass dishes with 2 mg/ml Pronase (Roche) dissolved in Danieu's buffer and later washed by E3 medium and transferred into agarose molds immersed in E3 medium. Some tens of cells from the donor embryos were transferred into the animal pole of the acceptors using a glass capillary. Acceptor embryos were then transferred to glass dishes with E3 medium supplemented with 100 U penicillin and streptomycin (Thermo Fisher Scientific) and kept at 32°C.

DNA and morpholino injection

DNA constructs were injected into the cytoplasm of one-cell-stage embryos. The DNA was diluted in double-distilled H_2O supplemented with 0.05% phenol red (Sigma-Aldrich). Injected volumes ranged from 0.5 to 1 nl. DNA concentrations ranged from 10 to 20 ng/µl and did not exceed 30 ng/µl even when multiple constructs were injected (*hsp70:EB3-mKate2*, 5 ng/µl). 0.5–1 ng *laminin α1* morpholino (5′-TCATCCTCATCTCCATCATCGCTCA-3′) or 0.5–1 ng of control morpholino (5′-CCTCTTACCTCAGTTACAATTTATA-3′) was injected together with 2–4 ng *p53* morpholino (5′-GCGCAATTGCTTTGCAAGAATGT-3′), an amount used previously (Randlett et al., 2011b). 2 ng *ath5* morpholino (5′-TTCATGGCTCTTCAAAAAAGTCTCC-3′) was used, an amount used previously (Pittman et al., 2008) to inhibit

RGC formation. All morpholinos were purchased from Gene Tools. 2 ng *p53* morpholino was also co-injected together with the *hsp70:Stathmin1-mKate2* and *hsp70:mKate2-NWASP-CA* constructs to alleviate the toxicity connected with construct overexpression.

DNA constructs used and cloning strategies

Gateway cloning (Thermo Fisher Scientific) based on the Tol2 kit (Kwan et al., 2007) was used for all constructs.

ath5:mKate2-aPKC-CAAX. The coding sequence of mKate2-aPKC-CAAX (Strzyz et al., 2015) was assembled by classical cloning in the pCS2+ backbone and used as a template for creating the mKate2-aPKC-CAAX middle entry clone by PCR using Phusion polymerase (New England Biolabs, Inc.) with the primers forward (5′-ggggacaagtttgtacaaaaaagcaggctggATGGTGAGCGAGCTGATTAAGG-3′) and reverse (5′-ggggaccactttgtacaagaaagctgggtcTTAGGAGAGCACACACTTG-3′). In all sequences, the lowercase letters refer to the ATT recombination site, whereas the uppercase letters refer to the complementary sequence to the gene.

The *ath5* promoter 5′ entry clone (Kwan et al., 2007) was combined with the mKate2-aPKC-CAAX middle entry clone and pTol2+pA R4-R2 backbone (Villefranc et al., 2007).

ath5:GFP-CAAX. The *ath5* promoter 5′ entry clone (Kwan et al., 2007) was combined with the GFP-CAAX middle entry clone (Kwan et al., 2007) and pTol2+pA R4-R2 backbone (Villefranc et al., 2007).

ath5:GFP-DCX. The coding sequence of human Doublecortin GFP-DCX plasmid was a gift from J. Gleeson (The Rockefeller University, New York, NY; plasmid 32852; Addgene; Tanaka et al., 2004). The GFP-DCX middle entry clone was created by PCR using Phusion polymerase with the primers forward (5′-ggggacaagtttgtacaaaaaagcaggctggATGGTGAGCAAGGGCGAGG-3′) and reverse (5′-ggggaccactttgtacaagaaagctgggtcTTACATGGAATCACCAAGCG-3′).

The GFP-DCX middle entry clone was combined with the *ath5* promoter 5′ entry clone (Kwan et al., 2007) and pTol2+pA R4-R2 backbone (Villefranc et al., 2007).

ath5:H2B-RFP. The H2B-RFP middle entry clone (Strzyz et al., 2015) was combined with the *ath5* promoter 5′ entry clone (Kwan et al., 2007) and pTol2+pA R4-R2 backbone (Villefranc et al., 2007).

bactin:GFP-DCX. The GFP-DCX middle entry clone used in this study was combined with the β-actin promoter 5′ entry clone (Kwan et al., 2007) and pTol2+pA R4-R2 backbone (Villefranc et al., 2007). The final construct was injected together with the Tol2 RNA to create the transgenic line.

bactin:mKate2-ras. The coding sequence of mKate2 with a membrane-targeting signal from *Homo sapiens* Harvey rat sarcoma viral oncogene homologue was used. The mKate2-ras middle entry

Table 1. **Transgenic lines**

Line	Structures labeled	Reference
Tg(bactin:GFP-DCX)	All MTs	This study
Tg(hsp70:mKate2-aPKC-CAAX)	aPKC in all membranes	This study
Tg(bactin:ras-GFP)	All membranes	Gift from C.P. Heisenberg laboratory[a]
Tg(ath5:gap-GFP)	Membranes of RGCs and photoreceptors	Zolessi et al., 2006
Tg(ath5:gap-RFP)	Membranes of RGCs and photoreceptors	Zolessi et al., 2006
Tg(crx:gap-CFP)	Membranes of photoreceptors and bipolar cells	Almeida et al., 2014
Tg(ptf1a:DsRed)	ACs and horizontal cells	Jusuf et al., 2012
Tg(ptf1a:Gal4-VP16, UAS:gap-YFP)	Membranes of ACs and horizontal cells	Pisharath and Parsons, 2009; Williams et al., 2010
Tg(SoFa2)	All retinal cells	Almeida et al., 2014
Tg(vsx1:GFP)	Bipolar cells	Kimura et al., 2008

[a]C.P. Heisenberg, Institute of Science and Technology Austria, Klosterneuburg, Austria.

clone was created by PCR using Phusion polymerase with the primers forward (5′-ggggacaagtttgtacaaaaaagcaggctggATGGTGAGCGAGCTG ATTAAGG-3′) and reverse (5′-ggggaccactttgtacaagaaagctgggtcTCA GGAGAGCACACACTTGC-3′).

The mKate2-ras middle entry clone (this study) was combined with the β-actin promoter 5′ entry clone (Kwan et al., 2007) and pTol2+pA R4-R2 backbone (Villefranc et al., 2007).

hsp70:Arl13b-mKate2. The coding sequence of human ADP-ribosylation factor-like protein 13B (Arl13b-mKate2) plasmid was a gift from B. Ciruna (University of Toronto, Toronto, Canada). The Arl13b-mKate2 middle entry clone was created by PCR using Phusion polymerase with the primers forward (5′-ggggacaagtttgtacaaaaaagcaggctggATGTTCAGTCTGATGGCC-3′) and reverse (5′-ggggaccactttgtacaagaaagctgggtcTTATTTGTGCCCCAG TTT-3′).

The Arl13b-mKate2 middle entry clone was combined with the *hsp70* promoter 5′ entry clone (Kwan et al., 2007) and pTol2+pA R4-R2 backbone (Villefranc et al., 2007).

pCS2+ Centrin-tdTomato. This construct was a gift from D. Gilmour (The European Molecular Biology Laboratory, Heidelberg, Germany).

hsp70:EB3-mKate2. To create the middle entry clone of human MT-associated protein EB3 (also called MAPRE3) tagged with mKate2, it was amplified from pCS2+ EB3-mKate2 (Strzyz et al., 2015) by PCR using Phusion polymerase with the primers forward (5′-ggggacaagtttgtacaaaaaagcaggctggATGGCCGTCAATGTGTAC TCC-3′) and reverse (5′-ggggaccactttgtacaagaaagctgggtcTCATCT GTGCCCCAGTTTGC-3′).

The EB3-mKate2 middle entry clone was combined with the *hsp70* promoter 5′ entry clone (Kwan et al., 2007) and pTol2+pA R4-R2 backbone (Villefranc et al., 2007).

hsp70:GalT-RFP. The GalT-RFP (N-terminal 61–amino acid fragment of human galactosyl transferase) plasmid was a gift from J. Lippincott-Schwartz (National Institutes of Health, Bethesda, MD). The GalT-RFP middle entry clone was created by PCR using Phusion polymerase with the primers forward (5′-ggggacaagtttgtacaaaaaagcaggctggATGAGGCTTCGGGAGCCGC-3′) and reverse (5′-ggggaccactttgtacaagaaagctgggtctTTAGGCGCCGGT GGAGTGG-3′).

The GalT-RFP middle entry clone was combined with the *hsp70* promoter 5′ entry clone (Kwan et al., 2007) and pTol2+pA R4-R2 backbone (Villefranc et al., 2007).

hsp70:mKate2-aPKC-CAAX. The construct was published previously (Strzyz et al., 2015). It was injected together with the Tol2 RNA to create the transgenic line.

hsp70:mKate2-NWASP-CA. The coding sequence of the zebrafish *wasb* gene was amplified from cDNA. The truncation was created based on homology with a previously published human construct (Rohatgi et al., 1999). The last 55 C-terminal amino acids act as dominant negative and inhibit the Arp2/3 complex. The NWASP-CA 3′ entry clone was created by PCR using Phusion polymerase with the primers forward (5′-ggggacagctttcttgtacaaagtggctGTGTCTGAATCC CCGGAC-3′) and reverse (5′-ggggacaactttgtataataaagttgcTTAGTC ATCCCATTCATCATCT-3′).

The NWASP-CA 3′ entry clone was combined with the *hsp70* promoter 5′ entry clone (Kwan et al., 2007), mKate2 middle entry clone (a gift from the A. Oates laboratory, Francis Crick Institute, London, England, UK), and pTol2+pA R4-R3 backbone (Kwan et al., 2007).

hsp70:PCNA-GFP. The coding sequence of human PCNA was used as a template. The EGFP-PCNA middle entry clone was created by PCR using Phusion polymerase with the primers forward (5′-ggggacaagtttgtacaaaaaagcaggctggATGGTGAGCAAGGGCGAGG-

3′) and reverse (5′-ggggaccactttgtacaagaaagctgggtcCTAAGATCCTTC TTCATCCTCG-3′).

The EGFP-PCNA middle entry clone was combined with the *hsp70* promoter 5′ entry clone (Kwan et al., 2007) and pTol2+pA R4-R2 backbone (Villefranc et al., 2007).

hsp70:Stathmin1-mKate2. The construct was published previously (Taverna et al., 2016).

Drug treatments

The necessary inhibitor concentration was determined based on previous studies in combination with a dilution series scanning for relevant phenotypes for all drug conditions. For CK-666 and Rockout, this is shown in Fig. S3 (D and E), and a similar experiment was performed for colcemid treatment. Higher drug concentrations were used when the embryos were mounted in agarose for imaging, compared with experiments when embryos were directly exposed to the medium with the drug. Colcemid (Enzo Life Sciences) was dissolved in DMSO as a 25-mM stock solution. The final concentration was 100 µM. CK-666 (Merck) was dissolved in DMSO as a 50-mM stock solution. The final concentration was 200 or 250 µM. Rockout (Santa Cruz Biotechnology, Inc.) was dissolved in DMSO as a 50-mM stock solution. The final concentration was 50 or 100 µM. Aphidicolin (Sigma-Aldrich) was dissolved in DMSO as a 30-mM stock solution. The final concentration was 150 µM. Hydroxyurea (Sigma-Aldrich) was dissolved in H_2O as a 1-M stock solution. The final concentration was 20 mM. All drug treatments were performed in 2 ml E3 medium in a 24-well plate or in a glass-bottom dish for live imaging experiments. The same volumes of DMSO served as a control. The treatments started at the onset of RGC specification at ~32 hpf and lasted until 48 hpf, when embryos were fixed for immunostaining, or until the end of live imaging experiment.

Immunofluorescence

All immunostainings were performed on whole-mount embryos fixed in 4% paraformaldehyde (Sigma-Aldrich) in PBS. The embryos were permeabilized with trypsin, blocked, and incubated with the primary antibody for 3 d. The Zn5 antibody (ZIRC, RRID:AB_10013770) was used at 1:50, the phosphorylated histone H3 antibody (ab10543, RRID:AB_2295065; Abcam) was used at 1:500, the acetylated tubulin antibody (T6793 RRID:AB_477585; Sigma-Aldrich) was used at 1:500, and the Laminin α1 antibody (L9393, RRID:AB_477163; Sigma-Aldrich) was used at 1:250. Next, embryos were incubated for 3 d with an appropriate fluorescently labeled secondary antibody (Molecular Probes) at 1:1,000 and DAPI or 5 µM DRAQ5 (Thermo Fisher Scientific). Phalloidin–Alexa Fluor 488 (Thermo Fisher Scientific) was used at 1:50. The acridine orange (Sigma-Aldrich) was dissolved at 2 µg/ml in E3 medium, and live embryos were incubated in the solution for 30 min followed by 10 brief washes with E3 medium and imaging with the GFP filter set.

Image acquisition

Confocal scans. Fixed samples were imaged in a laser-scanning microscope (LSM 510 or LSM 780; ZEISS) using the 40×/1.2 or 63×/1.2 C-Apochromat water immersion objective (ZEISS). The samples were mounted in 1% agarose in glass-bottom dishes (MatTek Corporation) filled with E3 medium and imaged at room temperature. The microscope was operated with the ZEN 2011 (black edition) software (ZEISS).

Time-lapse imaging using LSFM. Imaging was performed as previously described (Icha et al., 2016) using the Lightsheet Z.1 imaging system (ZEISS). In brief, the embryo was embedded in a 0.9% low melt agarose column, and a 50–80-µm z stack of each eye was acquired with 1-µm steps in a single view, dual-sided illumination mode. Images

were taken every 5 min for 12–16 h using the 10×/0.2 illumination objectives and a Plan-Apochromat 20×/1.0 W or 40×/1.0 W detection objective (all ZEISS) and the two Edge 5.5 sCMOS cameras (PCO). The microscope was operated with the ZEN 2014 (black edition) software (ZEISS). The sample chamber was filled with E3 medium containing 0.01% MS-222 (Sigma-Aldrich) and 0.2 mM *N*-phenylthiourea (Sigma-Aldrich) and maintained at 28.5°C.

Time-lapse imaging using spinning disk confocal microscopy. The spinning disk setup consisted of the IX71 microscope (Olympus) and the scan head CSU-X1 (Yokogawa Electric Corporation). The samples were mounted in glass-bottom dishes (MatTek Corporation) into 0.9% agarose in E3 medium containing 0.1 M Hepes, pH 7.25, and 0.01% MS-222 (Sigma-Aldrich). The dish was filled with E3 medium containing 0.01% MS-222 and 0.2 mM *N*-phenylthiourea. Imaging was performed with an UPLSAPO 60×/1.3 silicon oil objective (Olympus) and Neo sCMOS camera (Andor Technology) at 28.5°C regulated by an environmental chamber. A z stack around 30 μm thick was acquired with 1-μm steps every 5 or 10 min. The microscope was operated with the iQ 3.0 software (Andor Technology).

Image analysis. All the image data were processed in Fiji (Schindelin et al., 2012). The raw LSFM data were deconvolved in ZEN 2014 software (black edition, release version 9.0) using the Nearest Neighbor algorithm. The drift was corrected with a manual drift correction plugin (http://imagej.net/Manual_drift_correction_plugin, ImageJ). The apoptotic cells were counted automatically with an ImageJ script (see supplemental material). Prism (version 6.0c for Mac OS; GraphPad Software) was used for statistical analysis and to create graphs.

Cell trajectory, directionality ratio, and MSD analysis. The translocation of cells was tracked manually in 2D in maximum projected substacks of the raw data by following the center of the cell body in Fiji using the ImageJ plugin MtrackJ (Meijering et al., 2012). The resulting trajectories were analyzed as described previously (Norden et al., 2009; Leung et al., 2011) by calculating instantaneous velocities, MSDs, and directionality ratios. MSDs and directionality ratios were calculated in the DiPer program (Gorelik and Gautreau, 2014) executed as a macro in Excel (Microsoft). MSD values were fitted with $2D_{\Delta}t^{\alpha}$ to estimate the α. D represents the diffusion coefficient, and $_{\Delta}t$ is the interval between time points. The fit was done with nonlinear regression (least squares) in Prism.

Online supplemental material

Fig. S1 shows the comparison of RGC velocities and of mounting strategies in spinning disk microscopy and LSFM. It further displays organelle positions during RGC somal translocation. Fig. S2 shows quantifications of nuclear movement in RGCs compared with progenitors. Fig. S3 shows how RGC translocation is influenced by Laminin knockdown and control experiments for perturbations of the actin cytoskeleton. Fig. S4 shows control experiments for Stathmin and NWA SP-CA overexpression and additional quantification of RGC movement in these conditions. It also contains all the data on AC translocation. Fig. S5 shows control experiments for overexpression of the aPKC-CAAX construct. Video 1 shows somal translocation of RGCs with and without basal process and nuclear movements in progenitors as a comparison. Video 2 shows positions of centrosomes, primary cilia, and Golgi apparatus during RGC translocation. Video 3 shows how ROCK inhibition interferes with RGC translocation. Video 4 shows the distribution of MTs during RGC translocation. Video 5 shows all examples of rare wild-type, MT destabilization–induced, Arp2/3 inhibition–induced, and AC multipolar migration. Video 6 shows stalled RGC translocation upon aPKC-CAAX overexpression. Additionally, a script for detection of apoptotic cells is available as a Word file.
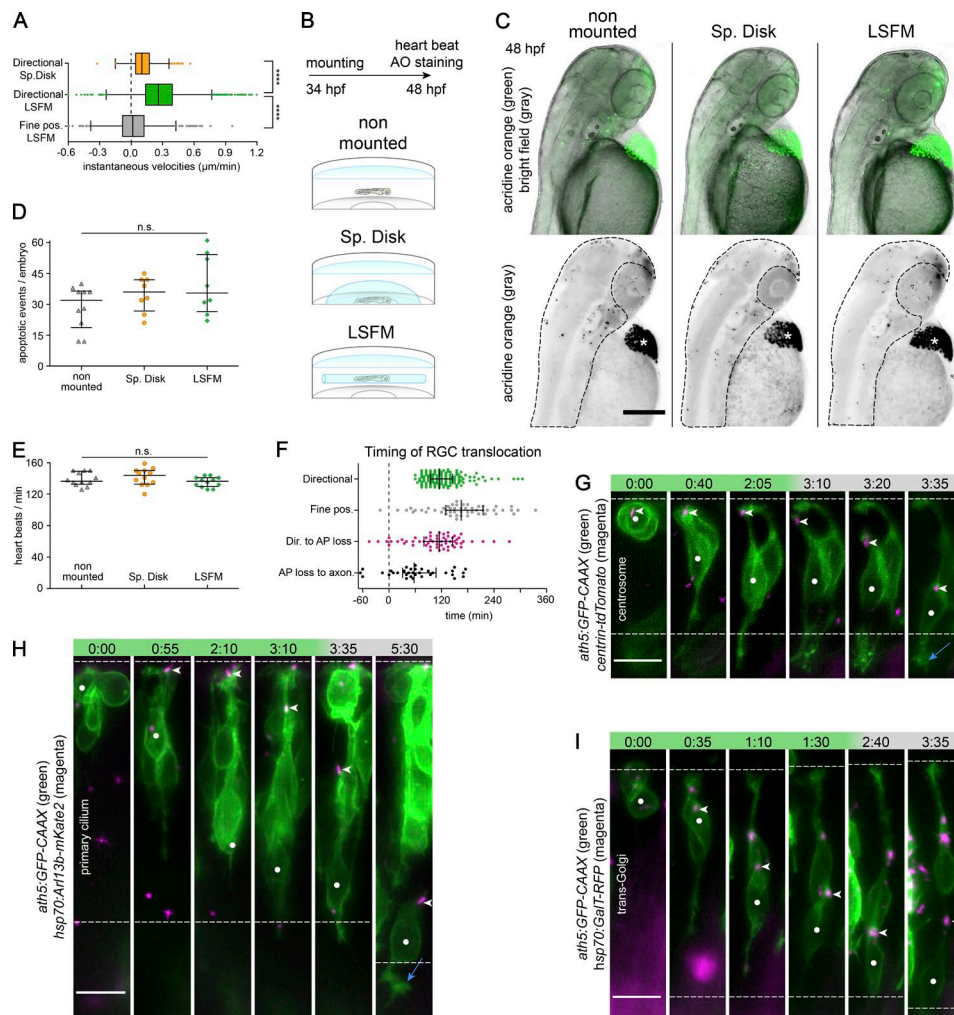
References

Almeida, A.D., H. Boije, R.W. Chow, J. He, J. Tham, S.C. Suzuki, and W.A. Harris. 2014. Spectrum of fates: a new approach to the study of the developing zebrafish retina. *Development.* 141:1971–1980. http://dx.doi.org/10.1242/dev.104760

Bellion, A., J.-P. Baudoin, C. Alvarez, M. Bornens, and C. Métin. 2005. Nucleokinesis in tangentially migrating neurons comprises two alternating phases: forward migration of the Golgi/centrosome associated with centrosome splitting and myosin contraction at the rear. *J. Neurosci.* 25:5691–5699. http://dx.doi.org/10.1523/JNEUROSCI.1030-05.2005

Brown, N.L., S. Kanekar, M.L. Vetter, P.K. Tucker, D.L. Gemza, and T. Glaser. 1998. Math5 encodes a murine basic helix-loop-helix transcription factor expressed during early stages of retinal neurogenesis. *Development.* 125:4821–4833.

Cajal, S.R. 1972. The Structure of the Retina. S.A. Thorpe, and M. Glickstein, editors. Charles Thomas, Springfield, Illinois. 196 pp.

Chow, R.W.-Y., A.D. Almeida, O. Randlett, C. Norden, and W.A. Harris. 2015. Inhibitory neuron migration and IPL formation in the developing zebrafish retina. *Development.* 142:2665–2677. http://dx.doi.org/10.1242/dev.122473

Cooper, J.A. 2013. Mechanisms of cell migration in the nervous system. *J. Cell Biol.* 202:725–734. http://dx.doi.org/10.1083/jcb.201305021

Distel, M., J.C. Hocking, K. Volkmann, and R.W. Köster. 2010. The centrosome neither persistently leads migration nor determines the site of axonogenesis in migrating neurons in vivo. *J. Cell Biol.* 191:875–890. (published erratum appears in *J. Cell Biol.* 2010. 191:875–890) http://dx.doi.org/10.1083/jcb.201004154

Driscoll, M.K., and G. Danuser. 2015. Quantifying modes of 3D cell migration. *Trends Cell Biol.* 25:749–759. http://dx.doi.org/10.1016/j.tcb.2015.09.010

Elias, L.A.B., D.D. Wang, and A.R. Kriegstein. 2007. Gap junction adhesion is necessary for radial migration in the neocortex. *Nature.* 448:901–907. http://dx.doi.org/10.1038/nature06063

Famulski, J.K., N. Trivedi, D. Howell, Y. Yang, Y. Tong, R. Gilbertson, and D.J. Solecki. 2010. Siah regulation of Pard3A controls neuronal cell adhesion during germinal zone exit. *Science.* 330:1834–1838. http://dx.doi.org/10.1126/science.1198480

Galli-Resta, L., P. Leone, D. Bottari, M. Ensini, E. Rigosi, and E. Novelli. 2008. The genesis of retinal architecture: an emerging role for mechanical interactions? *Prog. Retin. Eye Res.* 27:260–283. http://dx.doi.org/10.1016/j.preteyeres.2008.02.001

Gorelik, R., and A. Gautreau. 2014. Quantitative and unbiased analysis of directional persistence in cell migration. *Nat. Protoc.* 9:1931–1943. http://dx.doi.org/10.1038/nprot.2014.131

He, J., G. Zhang, A.D. Almeida, M. Cayouette, B.D. Simons, and W.A. Harris. 2012. How variable clones build an invariant retina. *Neuron.* 75:786–798. http://dx.doi.org/10.1016/j.neuron.2012.06.033

Hinds, J.W., and P.L. Hinds. 1974. Early ganglion cell differentiation in the mouse retina: an electron microscopic analysis utilizing serial sections. *Dev. Biol.* 37:381–416. http://dx.doi.org/10.1016/0012-1606(74)90156-0

Huisken, J., J. Swoger, F. Del Bene, J. Wittbrodt, and E.H.K. Stelzer. 2004. Optical sectioning deep inside live embryos by selective plane illumination microscopy. *Science.* 305:1007–1009. http://dx.doi.org/10.1126/science.1100035

Icha, J., C. Schmied, J. Sidhaye, P. Tomancak, S. Preibisch, and C. Norden. 2016. Using light sheet fluorescence microscopy to image zebrafish eye development. *J. Vis. Exp.* 110:e53966. http://dx.doi.org/10.3791/53966

Jemielita, M., M.J. Taormina, A. Delaurier, C.B. Kimmel, and R. Parthasarathy. 2012. Comparing phototoxicity during the development of a zebrafish craniofacial bone using confocal and light sheet fluorescence microscopy techniques. *J. Biophotonics.* 6:920–928. http://dx.doi.org/10.1002/jbio.201200144

Jourdain, L., P. Curmi, A. Sobel, D. Pantaloni, and M.F. Carlier. 1997. Stathmin: a tubulin-sequestering protein which forms a ternary T_2S complex with two tubulin molecules. *Biochemistry.* 36:10817–10821. http://dx.doi.org/10.1021/bi971491b

Jusuf, P.R., S. Albadri, A. Paolini, P.D. Currie, F. Argenton, S. Higashijima, W.A. Harris, and L. Poggi. 2012. Biasing amacrine subtypes in the Atoh7 lineage through expression of Barhl2. *J. Neurosci.* 32:13929–13944. http://dx.doi.org/10.1523/JNEUROSCI.2073-12.2012

Kay, J.N., K.C. Finger-Baier, T. Roeser, W. Staub, and H. Baier. 2001. Retinal ganglion cell genesis requires *lakritz*, a Zebrafish *atonal* homolog. *Neuron.* 30:725–736. http://dx.doi.org/10.1016/S0896-6273(01)00312-9

Kay, J.N., T. Roeser, J.S. Mumm, L. Godinho, A. Mrejeru, R.O.L. Wong, and H. Baier. 2004. Transient requirement for ganglion cells during assembly of retinal synaptic layers. *Development.* 131:1331–1342. http://dx.doi.org/10.1242/dev.01040

Kay, J.N., B.A. Link, and H. Baier. 2005. Staggered cell-intrinsic timing of *ath5* expression underlies the wave of ganglion cell neurogenesis in the zebrafish retina. *Development.* 132:2573–2585. http://dx.doi.org/10.1242/dev.01831

Kimura, Y., C. Satou, and S. Higashijima. 2008. V2a and V2b neurons are generated by the final divisions of pair-producing progenitors in the zebrafish spinal cord. *Development.* 135:3001–3005. http://dx.doi.org/10.1242/dev.024802

Kwan, K.M., E. Fujimoto, C. Grabher, B.D. Mangum, M.E. Hardy, D.S. Campbell, J.M. Parant, H.J. Yost, J.P. Kanki, and C.-B. Chien. 2007. The Tol2kit: a multisite gateway-based construction kit for *Tol2* transposon transgenesis constructs. *Dev. Dyn.* 236:3088–3099. http://dx.doi.org/10.1002/dvdy.21343

Lam, P.-Y., S. Mangos, J.M. Green, J. Reiser, and A. Huttenlocher. 2015. In vivo imaging and characterization of actin microridges. *PLoS One.* 10:e0115639. http://dx.doi.org/10.1371/journal.pone.0115639

LeDizet, M., and G. Piperno. 1986. Cytoplasmic microtubules containing acetylated alpha-tubulin in *Chlamydomonas reinhardtii*: spatial arrangement and properties. *J. Cell Biol.* 103:13–22. http://dx.doi.org/10.1083/jcb.103.1.13

Lepanto, P., C. Davison, G. Casanova, J.L. Badano, and F.R. Zolessi. 2016. Characterization of primary cilia during the differentiation of retinal ganglion cells in the zebrafish. *Neural Dev.* 11:10. http://dx.doi.org/10.1186/s13064-016-0064-z

Leung, L., A.V. Klopper, S.W. Grill, W.A. Harris, and C. Norden. 2011. Apical migration of nuclei during G2 is a prerequisite for all nuclear motion in zebrafish neuroepithelia. *Development.* 138:5003–5013. http://dx.doi.org/10.1242/dev.071522

Marín, O., M. Valiente, X. Ge, and L.H. Tsai. 2010. Guiding neuronal cell migrations. *Cold Spring Harb. Perspect. Biol.* 2. http://dx.doi.org/10.1101/cshperspect.a001834

Martinez-Morales, J.R., M. Rembold, K. Greger, J.C. Simpson, K.E. Brown, R. Quiring, R. Pepperkok, M.D. Martin-Bermudo, H. Himmelbauer, and J. Wittbrodt. 2009. *ojoplano*-mediated basal constriction is essential for optic cup morphogenesis. *Development.* 136:2165–2175. http://dx.doi.org/10.1242/dev.033563

Masai, I., Z. Lele, M. Yamaguchi, A. Komori, A. Nakata, Y. Nishiwaki, H. Wada, H. Tanaka, Y. Nojima, M. Hammerschmidt, et al. 2003. N-cadherin mediates retinal lamination, maintenance of forebrain compartments and patterning of retinal neurites. *Development.* 130:2479–2494. http://dx.doi.org/10.1242/dev.00465

Meijering, E., O. Dzyubachyk, and I. Smal. 2012. Methods for cell and particle tracking. *Methods Enzymol.* 504:183–200. http://dx.doi.org/10.1016/B978-0-12-391857-4.00009-4

Nadarajah, B., J.E. Brunstrom, J. Grutzendler, R.O. Wong, and A.L. Pearlman. 2001. Two modes of radial migration in early development of the cerebral cortex. *Nat. Neurosci.* 4:143–150. http://dx.doi.org/10.1038/83967

Nawrocki, L.W. 1985. Development of the neural retina in the zebrafish, Brachydanio rerio (neurogenesis). PhD thesis. University of Oregon, Eugene, Oregon.

Noctor, S.C., V. Martínez-Cerdeño, L. Ivic, and A.R. Kriegstein. 2004. Cortical neurons arise in symmetric and asymmetric division zones and migrate through specific phases. *Nat. Neurosci.* 7:136–144. http://dx.doi.org/10.1038/nn1172

Nolen, B.J., N. Tomasevic, A. Russell, D.W. Pierce, Z. Jia, C.D. McCormick, J. Hartman, R. Sakowicz, and T.D. Pollard. 2009. Characterization of two classes of small molecule inhibitors of Arp2/3 complex. *Nature.* 460:1031–1034. http://dx.doi.org/10.1038/nature08231

Norden, C., S. Young, B.A. Link, and W.A. Harris. 2009. Actomyosin is the main driver of interkinetic nuclear migration in the retina. *Cell.* 138:1195–1208. http://dx.doi.org/10.1016/j.cell.2009.06.032

Okamoto, M., T. Namba, T. Shinoda, T. Kondo, T. Watanabe, Y. Inoue, K. Takeuchi, Y. Enomoto, K. Ota, K. Oda, et al. 2013. TAG-1–assisted progenitor elongation streamlines nuclear migration to optimize subapical crowding. *Nat. Neurosci.* 16:1556–1566. http://dx.doi.org/10.1038/nn.3525

Pisharath, H., and M.J. Parsons. 2009. Nitroreductase-mediated cell ablation in transgenic zebrafish embryos. *In* Zebrafish, Methods in Molecular Biology. Volume 546. G.J. Lieschke, A.C. Oates, and K. Kawakami, editors. Humana Press, Totowa, NJ. 133–143. http://dx.doi.org/10.1007/978-1-60327-977-2_9

Pittman, A.J., M.Y. Law, and C.B. Chien. 2008. Pathfinding in a large vertebrate axon tract: isotypic interactions guide retinotectal axons at multiple choice points. *Development.* 135:2865–2871. http://dx.doi.org/10.1242/dev.025049

Poggi, L., M. Vitorino, I. Masai, and W.A. Harris. 2005. Influences on neural lineage and mode of division in the zebrafish retina in vivo. *J. Cell Biol.* 171:991–999. http://dx.doi.org/10.1083/jcb.200509098

Randlett, O., C. Norden, and W.A. Harris. 2011a. The vertebrate retina: a model for neuronal polarization in vivo. *Dev. Neurobiol.* 71:567–583. http://dx.doi.org/10.1002/dneu.20841

Randlett, O., L. Poggi, F.R. Zolessi, and W.A. Harris. 2011b. The oriented emergence of axons from retinal ganglion cells is directed by laminin contact in vivo. *Neuron.* 70:266–280. http://dx.doi.org/10.1016/j.neuron.2011.03.013

Rohatgi, R., L. Ma, H. Miki, M. Lopez, T. Kirchhausen, T. Takenawa, and M.W. Kirschner. 1999. The interaction between N-WASP and the Arp2/3 complex links Cdc42-dependent signals to actin assembly. *Cell.* 97:221–231. http://dx.doi.org/10.1016/S0092-8674(00)80732-1

Saito, K., A. Kawaguchi, S. Kashiwagi, S. Yasugi, M. Ogawa, and T. Miyata. 2003. Morphological asymmetry in dividing retinal progenitor cells. *Dev. Growth Differ.* 45:219–229. http://dx.doi.org/10.1046/j.1524-4725.2003.690.x

Schindelin, J., I. Arganda-Carreras, E. Frise, V. Kaynig, M. Longair, T. Pietzsch, S. Preibisch, C. Rueden, S. Saalfeld, B. Schmid, et al. 2012. Fiji: an open-source platform for biological-image analysis. *Nat. Methods.* 9:676–682. http://dx.doi.org/10.1038/nmeth.2019

Sidman, R.L. 1961. Histogenesis of mouse retina studied with thymidine-H3. *In* Structure of the Eye. G.K. Smelser, editor. Academic Press, New York. 487–506.

Solecki, D.J., L. Model, J. Gaetz, T.M. Kapoor, and M.E. Hatten. 2004. Par6α signaling controls glial-guided neuronal migration. *Nat. Neurosci.* 7:1195–1203. http://dx.doi.org/10.1038/nn1332

Stelzer, E.H.K. 2015. Light-sheet fluorescence microscopy for quantitative biology. *Nat. Methods.* 12:23–26. http://dx.doi.org/10.1038/nmeth.3219

Stepanova, T., J. Slemmer, C.C. Hoogenraad, G. Lansbergen, B. Dortland, C.I. De Zeeuw, F. Grosveld, G. van Cappellen, A. Akhmanova, and N. Galjart. 2003. Visualization of microtubule growth in cultured neurons via the use of EB3-GFP (end-binding protein 3-green fluorescent protein). *J. Neurosci.* 23:2655–2664.

Strzyz, P.J., H.O. Lee, J. Sidhaye, I.P. Weber, L.C. Leung, and C. Norden. 2015. Interkinetic nuclear migration is centrosome independent and ensures

apical cell division to maintain tissue integrity. *Dev. Cell.* 32:203–219. http://dx.doi.org/10.1016/j.devcel.2014.12.001

Tabata, H., and K. Nakajima. 2003. Multipolar migration: the third mode of radial neuronal migration in the developing cerebral cortex. *J. Neurosci.* 23:9996–10001.

Tanaka, T., F.F. Serneo, C. Higgins, M.J. Gambello, A. Wynshaw-Boris, and J.G. Gleeson. 2004. Lis1 and doublecortin function with dynein to mediate coupling of the nucleus to the centrosome in neuronal migration. *J. Cell Biol.* 165:709–721. http://dx.doi.org/10.1083/jcb.200309025

Taverna, E., F. Mora-Bermúdez, P.J. Strzyz, M. Florio, J. Icha, C. Haffner, C. Norden, M. Wilsch-Bräuninger, and W.B. Huttner. 2016. Non-canonical features of the Golgi apparatus in bipolar epithelial neural stem cells. *Sci. Rep.* 6. http://dx.doi.org/10.1038/srep21206

Trevarrow, B., D.L. Marks, and C.B. Kimmel. 1990. Organization of hindbrain segments in the zebrafish embryo. *Neuron.* 4:669–679. http://dx.doi.org/10.1016/0896-6273(90)90194-K

Tsai, J.-W., K.H. Bremner, and R.B. Vallee. 2007. Dual subcellular roles for LIS1 and dynein in radial neuronal migration in live brain tissue. *Nat. Neurosci.* 10:970–979. http://dx.doi.org/10.1038/nn1934

Umeshima, H., T. Hirano, and M. Kengaku. 2007. Microtubule-based nuclear movement occurs independently of centrosome positioning in migrating neurons. *Proc. Natl. Acad. Sci. USA.* 104:16182–16187. http://dx.doi.org/10.1073/pnas.0708047104

Villefranc, J.A., J. Amigo, and N.D. Lawson. 2007. Gateway compatible vectors for analysis of gene function in the zebrafish. *Dev. Dyn.* 236:3077–3087. http://dx.doi.org/10.1002/dvdy.21354

Wang, P.-S., F.-S. Chou, S. Ramachandran, S. Xia, H.-Y. Chen, F. Guo, P. Suraneni, B.J. Maher, and R. Li. 2016. Crucial roles of the Arp2/3 complex during mammalian corticogenesis. *Development.* 143:2741–2752. http://dx.doi.org/10.1242/dev.130542

Williams, P.R., S.C. Suzuki, T. Yoshimatsu, O.T. Lawrence, S.J. Waldron, M.J. Parsons, M.L. Nonet, and R.O.L. Wong. 2010. In vivo development of outer retinal synapses in the absence of glial contact. *J. Neurosci.* 30:11951–11961. http://dx.doi.org/10.1523/JNEUROSCI.3391-10.2010

Yanagida, M., R. Miyoshi, R. Toyokuni, Y. Zhu, and F. Murakami. 2012. Dynamics of the leading process, nucleus, and Golgi apparatus of migrating cortical interneurons in living mouse embryos. *Proc. Natl. Acad. Sci. USA.* 109:16737–16742. http://dx.doi.org/10.1073/pnas.1209166109

Zolessi, F.R., L. Poggi, C.J. Wilkinson, C.-B. Chien, and W.A. Harris. 2006. Polarization and orientation of retinal ganglion cells in vivo. *Neural Dev.* 1:2. http://dx.doi.org/10.1186/1749-8104-1-2

Figure S1.   **Mounting is not responsible for differences between LSFM and spinning disk microscopy.** Organelle positions during RGC somal translocation. (A) Comparison of instantaneous velocities during RGC directional phase between the spinning disk confocal microscope and LSFM and between directional phase and fine positioning phases in LSFM. The values are taken from the first 95 min (or less) after mitosis or from the first 95 min of the fine positioning. The instantaneous velocities are calculated from the 1D movement along the apico–basal axis of the retina. The movement from apical to basal has a positive sign; the reverse movement has a negative sign. Directional spin disk, n = 21 and 4, 399 data points; directional LSFM, n = 140 and 24, 2,587 data points; and fine positioning LSFM, n = 83 and 22, 1,539 data points. 38 outliers were discarded by ROUT (Q = 1.0%) for the plotting purposes but not for the statistical testing, which was done on the whole dataset. The differences between instantaneous velocities are statistically significant: directional LSFM versus fine positioning LSFM. Mann-Whitney U test; ****, $P < 0.0001$; directional LSFM versus directional spin disk; Mann-Whitney U test, $P < 0.0001$. The data are shown as a Tukey boxplot (box shows median and interquartile range, and whiskers show 1.5 of the interquartile range). The median instantaneous velocity of directional spin disk = 0.101 µm/min, directional LSFM = 0.261 µm/min, and fine positioning LSFM = 0.015 µm/min. (B) Scheme of the experiment testing the influence of mounting for different microscopes on fish viability. The identical composition of E3 medium and agarose was used for both spin disk and LSFM mounting, and the dishes were kept together in an incubator overnight at 28.5°C. (C) Acridine orange (AO) staining for apoptotic cells. The maximum intensity projection is shown for acridine orange staining. The bright field image was created with the extended depth of field plugin in Fiji. Dashed area, area of apoptotic events count; asterisks, hatching gland. Bar, 200 µm. (D) The number of apoptotic events does not differ among the mounting strategies. n = 10, 8, and 8 fish, respectively. Median nonmounted = 32 events; median spin disk = 36 events; median LSFM = 36 events. Analysis of variance, P = 0.1458. (E) Heart rate does not differ among the mounting strategies. Heartbeats were counted manually for 20 s in 12 fish for each condition. Median nonmounted = 137 beats/min; median spin disk = 144 beats/min; median LSFM = 137 beats/min. Analysis of variance, P = 0.2149. (D and E) Bars represent median and interquartile range. n.s., not significant. (F) Timing of key events during RGC translocation. The duration of directional phase: median, 115 min (n = 140 and 24). The duration of fine positioning phase, i.e., the time from the end of directional movement to axonogenesis: median, 165 min (n = 50 and 19). The time from the end of directional phase to apical process (AP) loss: median, 115 min (n = 58 and 21). The time from apical process loss to axonogenesis: median, 57.5 min (n = 33 and 16). The whiskers show median and interquartile range. (G) Centrosome position during RGC translocation. *centrin-tdTomato* DNA was injected to label the centrosome together with *ath5:GFP-CAAX*. (H) Primary cilium position during RGC translocation. *hsp70:Arl13b-mKate2* DNA was injected to label primary cilium together with *ath5:GFP-CAAX*. (I) Golgi apparatus position during RGC translocation. Galactosyl transferase fragment *hsp70:GalT-RFP* DNA was injected to label trans-Golgi together with *ath5:GFP-CAAX*. (G–I) Green phase, directional movement; gray phase, fine positioning. Dashed lines delimit the apical and basal sides of the retina. White dots, RGC followed; arrowheads, organelle followed; blue arrows, axons. Time is shown in hours and minutes. Bars, 10 µm.
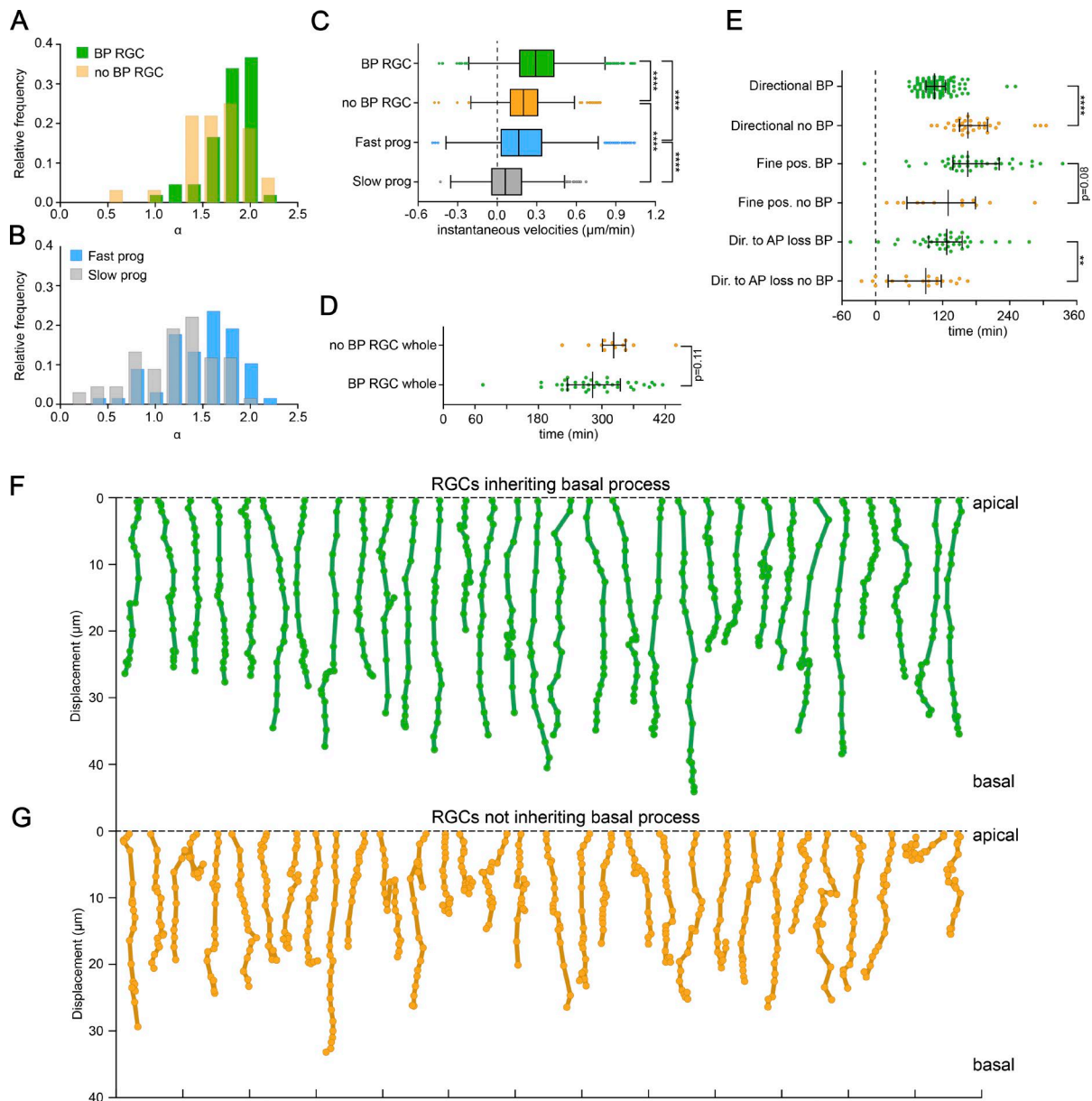
Figure S2. **Quantifications of nuclear movement in RGCs and progenitors.** (A) The α value distribution from MSDs of RGCs inheriting and not inheriting the basal process (BP) in the directional phase (data from Fig. 2 G). Median basal process RGCs = 1.83; no basal process RGCs = 1.70. The differences between α values are statistically significant: basal process RGCs versus no basal process RGCs, Mann-Whitney *U* test, P = 0.03. (B) The α value distribution from MSDs of fast and slow progenitor nuclei after mitosis (data from Fig. 2 H). Median fast progenitor = 1.53; slow progenitor = 1.26. The differences between α values are statistically significant: fast progenitors versus slow progenitors, Wilcoxon matched pairs signed rank test, P < 0.0001. (C) Comparison of instantaneous velocities among cells inheriting and not inheriting the basal process in directional phase (after mitosis). The values are taken from the first 70 min after mitosis. The instantaneous velocities are calculated from the 1D movement along the apico–basal axis of the retina. The movement from apical to basal has a positive sign; the reverse movement has a negative sign. Basal process RGC, *n* = 109 and 23, 1,526 data points; no basal process RGC, *n* = 31 and 19,448 data points; fast progenitor, *n* = 68 and 7,952 data points; slow progenitor, *n* = 68 and 7,952 data points. 45 outliers were discarded by ROUT (Q = 1.0%) for the plotting purposes, not for the statistical testing, which was done on the whole dataset. The differences between instantaneous velocities are statistically significant: basal process RGCs versus no basal process RGCs, Mann-Whitney *U* test, P < 0.0001; fast progenitors versus slow progenitors, Wilcoxon matched pairs signed rank test, P < 0.0001; no basal process RGCs versus slow progenitors, Mann-Whitney *U* test, P < 0.0001; basal process RGCs versus fast progenitors, Mann-Whitney *U* test, P < 0.0001. The data are shown as a Tukey boxplot (box shows median and interquartile ranges, and whiskers show 1.5 of the interquartile range). The median basal process RGCs = 0.29 µm/min, no BP RGCs = 0.20 µm/min, fast progenitors = 0.16 µm/min, slow progenitors = 0.06 µm/min. (D) Timing of the whole RGC translocation event (from mitosis to axonogenesis) in RGCs with and without basal process. Basal process median = 282.5 min (*n* = 38 and 18); no basal process median = 322.5 min (*n* = 12and 9); Mann-Whitney *U* test, P = 0.11. (E) Timing of events during RGC translocation depending on the basal process inheritance. Median values: directional basal process = 105 min (*n* = 109 and 23); directional no basal process = 165 min (*n* = 31 and 19); Mann-Whitney *U* test, **, P < 0.01; ****, P < 0.0001. Median values: fine positioning basal process = 165 min (*n* = 38 and 18), fine positioning no basal process = 130 min (*n* = 12 and 9); Mann-Whitney *U* test, P = 0.08. Median values: from end of directional phase to apical process loss, basal process = 127.5 min (*n* = 38 and 16); no basal process = 90 min (*n* = 20 and 15); Mann-Whitney *U* test, P = 0.003. (D and E) The median and interquartile ranges are shown. (F and G) Trajectories of RGCs inheriting (F) and not inheriting (G) the basal process. The representative 2D trajectories of 31 RGCs inheriting the basal process (F) or not (G) were plotted as manually tracked over the first 95 min after the terminal division.
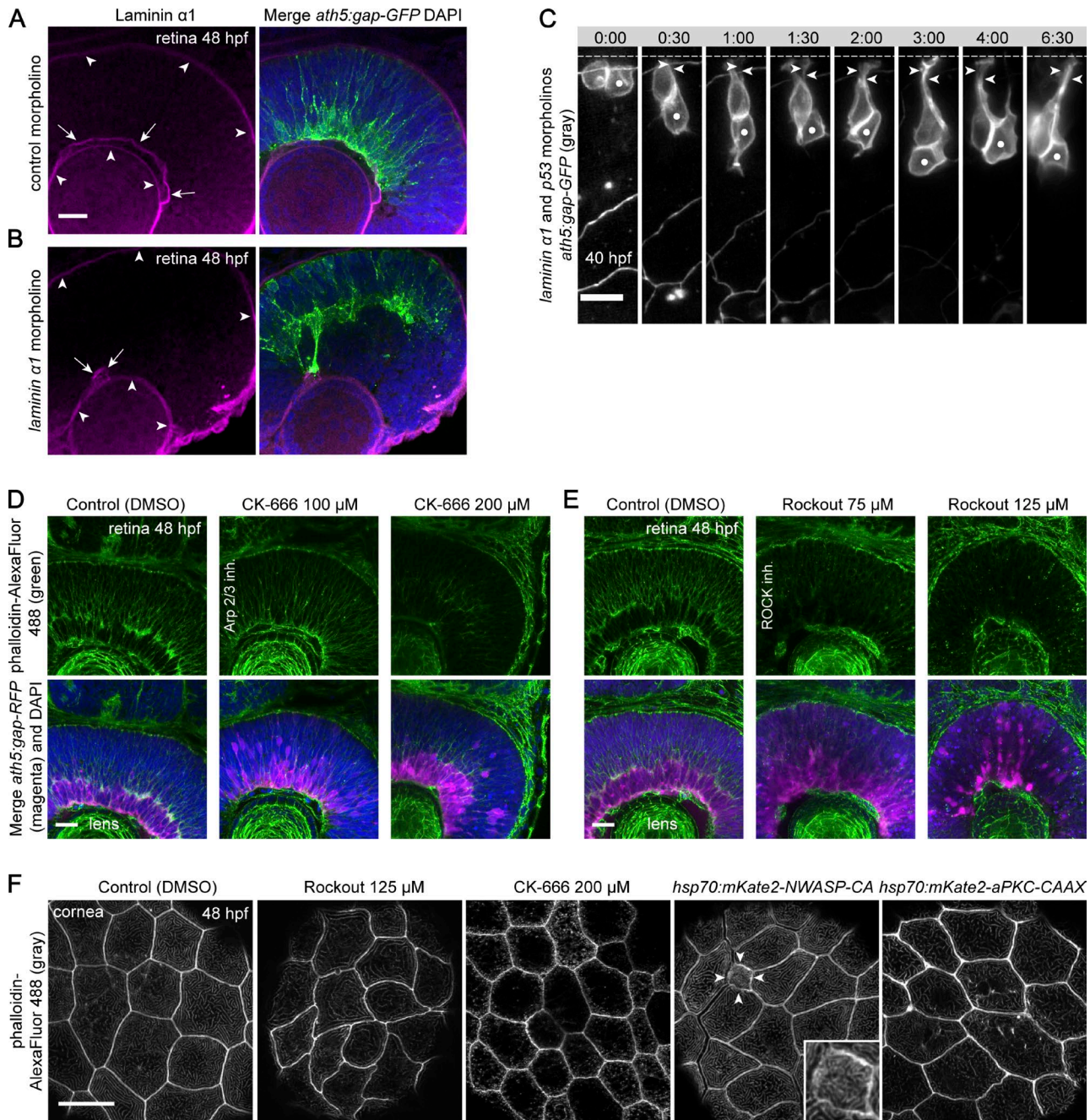
Figure S3. **RGC translocation is influenced by Laminin knockdown.** Control experiments for actin perturbations. (A) Laminin α1 distribution in control retina at 48 hpf. The Laminin channel was denoised in Fiji (ROF denoise). Note the three distinct layers of Laminin (magenta) in the developing eye and the RGCs (green) forming a basal layer of the retina. Bar, 20 μm. (B) Laminin α1 distribution after Laminin knockdown. Note that Laminin is still present in the lens and basal membrane of the retinal pigment epithelium, but is mostly absent in the retinal basal membrane, causing a tissue-wide lamination problem with the RGC layer forming in the central retina. Note that axons of RGCs associate with a small patch of Laminin left in the retinal basal membrane. (A and B) Arrows, Laminin in retina basal membrane; arrowheads, Laminin in lens and basal membrane of the retinal pigment epithelium. (C) RGC translocation is perturbed after Laminin α1 knockdown. Note that after division, the cells lose the basal process and do not translocate basally. Dashed lines delimit the apical side of the retina. White dots, RGC followed; arrowheads, apical process. Time is shown in hours and minutes. Bar, 10 μm. (D) Effect of Arp2/3 inhibition on actin cytoskeleton in the retina. Note the decreased actin staining in the 200-μM condition in the basal and central retina. The apical actin belt associated with adherens junctions is less affected. The RGC layer labeled by *ath5:gap-RFP* is disorganized. (E) Effect of ROCK inhibition on actin cytoskeleton in the retina. Note the decreased actin staining in the 75-μM and 125-μM conditions in the basal and central retina. The apical actin belt associated with adherens junctions is less affected. The RGC layer labeled by *ath5:gap-RFP* is disorganized. (F) Staining of apical actin by phalloidin in corneal cells at 48 hpf. Actin is present as two structures: it is associated with adherens junctions around the cell membranes and in microridges all over the apical membrane. The embryos were incubated with the inhibitors from 34 hpf (or heat shocked at 32 hpf) and analyzed at 48 hpf. (D–F) Bars, 20 μm. Rockout: Note that even at high Rockout concentration, the microridges persist. The cell shape, on the other hand, is more irregular compared with the control. CK-666: note the complete absence of microridges and reduced apical area of cells. NWASP-CA overexpression: this construct was injected mosaically, and the affected cell is marked with arrowheads and is shown in the inset. Note the massively reduced apical area and altered structure of microridges. aPKC-CAAX overexpression: note the altered shape of microridges and high accumulation of actin associated with adherens junctions compared with the control.
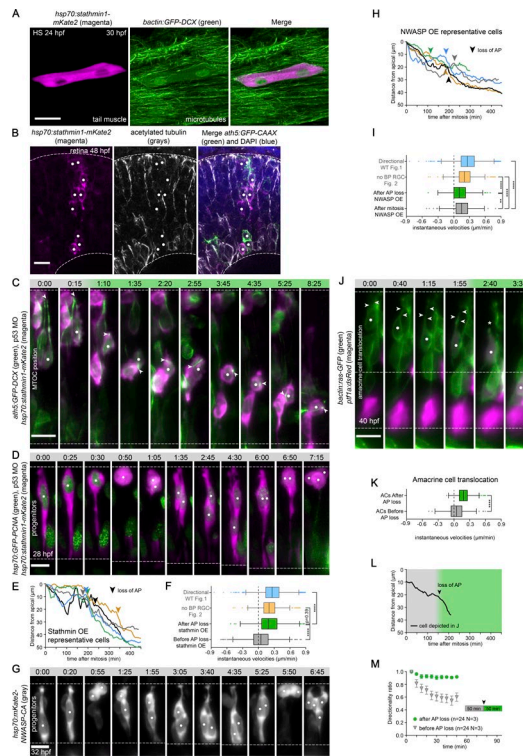
Figure S4. **Free migration of RGCs after MT destabilization or Arp2/3 inhibition and free migration of ACs.** (A) The destabilizing effect of the *hsp70 :Stathmin1-mKate2* construct on MTs. The embryos of transgenic line ubiquitously expressing GFP-tagged doublecortin to label MTs were injected with *hsp70:Stathmin1-mKate2*. The fish were heat shocked (HS) around 24 hpf and imaged live 6 h later. Note the diffuse GFP-DCX signal and absence of MT filaments in the affected cell. Bar, 20 µm. (B) Stathmin overexpression decreases MT acetylation. White dots, Stathmin-overexpressing cells. Bar, 10 µm. (C) Random MT-organizing center (MTOC) position during RGC multipolar migration. MTs and MT-organizing centers were labeled by *ath5:GFP-DCX* injection. The RGC (white dots) initially has an apical MTOC (white arrowheads). The loss of apical process attachment triggers the multipolar migratory mode (time 1:10), and later the MTOC is found at a random position in the cell. Gray phase, cell still has the apical process; green phase, directional multipolar mode. The dashed lines delimit the apical and basal sides of the retina. (D) MT depolymerization by *hsp70:Stathmin1-mKate2* has no effect on the retinal progenitor cell cycle or nuclear migration. The *ath5:gap-GFP* transgenic fish were injected with the *hsp70:Stathmin1-mKate2* and *hsp70:GFP-PCNA* DNA to label nuclei. At 7:15, the *ath5:gap-GFP* expression starts. (E) Five representative trajectories of the free migrating RGCs in the Stathmin overexpression (OE) condition. 0 indicates the mitotic position of cells. The arrowheads mark the time points when the cell loses the apical process. (F) Comparison of instantaneous velocities in Stathmin overexpression before and during the multipolar migration and with control conditions. The instantaneous velocities are calculated from the 1D movement along the apico–basal axis of the retina. The movement from apical to basal has a positive sign; the reverse movement has a negative sign. Directional wild type (WT; Fig. 1), *n* = 140 and 24,2587 data points; no basal process (BP) RGC (Fig. 2), *n* = 31 and 19,448 data points; after apical process (AP) loss Stathmin overexpression (OE), *n* = 32 and 5,631 data points; before apical process loss Stathmin overexpression, *n* = 32 and 5,919 data points. Statistical significance of the differences between instantaneous velocities: directional wild type (Fig. 1) versus after apical process loss Stathmin overexpression, Mann-Whitney *U* test, P < 0.0001; after apical process loss Stathmin overexpression versus before apical process loss Stathmin, Wilcoxon matched pairs signed rank test, P < 0.0001; no basal process RGC (Fig. 2) versus after apical process loss Stathmin overexpression, Mann-Whitney *U* test, P < 0.3956. The median directional wild type (Fig. 1) = 0.26 µm/min; no basal process RGCs (Fig. 2) = 0.20 µm/min; after apical process loss Stathmin = 0.18 µm/min; before apical process loss Stathmin = 0.05 µm/min. (G) Arp2/3 inhibition by NWASP-CA has no effect on the retinal progenitor cell cycle or nuclear migration. Wild-type fish were injected with *hsp70:mKate2-NWASP-CA* and *ath5:GFP-CAAX* (not expressed in these cells) DNA. (H) Five representative trajectories of the free migrating RGCs in the NWASP-CA overexpression condition. 0 indicates the mitotic position of cells. The arrowheads mark the time points when the cell loses its apical process. (I) Comparison of instantaneous velocities in NWASP-CA overexpression before and during the multipolar migration and with control conditions. The instantaneous velocities are calculated from the trajectories of cells 95 min after mitosis and 95 after apical process loss. After apical process loss NWASP overexpression, *n* = 18 and 4,342 data points; after mitosis NWASP overexpression, *n* = 18 and 4,342 data points. Statistical significance of the differences between instantaneous velocities: directional wild type (Fig. 1) versus after mitosis NWASP overexpression, Mann-Whitney *U* test, P < 0.0001; after apical process loss NWASP overexpression versus after mitosis NWA SP overexpression, Mann-Whitney *U* test, P = 0.0013; no basal process RGC (Fig. 2) versus after apical process loss NWASP overexpression, Mann-Whitney *U* test, P < 0.0001; no basal process RGC (Fig. 2) versus after mitosis NWASP overexpression, Mann-Whitney *U* test, P < 0.0001. The median after apical process loss NWASP overexpression = 0.10 µm/min; after mitosis NWASP overexpression = 0.15 µm/min. (F and I) Outliers were discarded by ROUT (Q = 1.0%) for the plotting purposes but not for the statistical testing, which was done on the whole dataset. **, P < 0.01. (J) AC translocation. *bactin:ras-GFP, ptf1a:dsRed* double transgenic embryos were used as donors for blastomere transplantation into wild-type acceptors. The translocating AC (white dots) initially has the apical process (white arrowheads). Once it is lost (asterisk), fast directional movement to its final position is triggered. Gray phase, still with apical process; green phase, directional multipolar mode. The dashed lines delimit the apical side of the retina and the inner nuclear layer, where the ACs reside. (D, E, G, and J) Time is shown in hours and minutes. Bars, 10 µm. (K) Comparison of instantaneous velocities in ACs before and after apical process loss. Four outliers were discarded by ROUT (Q = 1.0%). ACs after apical process loss, *n* = 24 and 3,257 data points; ACs before apical process loss, *n* = 24 and 3,462 data points. The differences between instantaneous velocities are statistically significant: ACs after apical process loss versus ACs before apical process loss, Mann-Whitney *U* test, ****, P < 0.0001. The median ACs after apical process loss = 0.18 µm/min; ACs before apical process loss = 0.05 µm/min. (F, I, and K) The data are shown as a Tukey boxplot (box shows median and interquartile ranges, and whiskers show 1.5 of the interquartile range). (L) A representative trajectory of the translocating AC from J. The arrowhead marks the time point when the cell loses the apical process. (M) Directionality ratio of ACs before and after apical process loss. The mean of all tracks is shown with error bars representing the SEM. The interval of 50 min before and 50 min after AP loss was taken into account (arrowhead), because that is the mean duration of the directional movement after apical process loss in ACs. Final directionality ratio: ACs after apical process loss = 0.92 ACs; before apical process loss = 0.60 ACs.
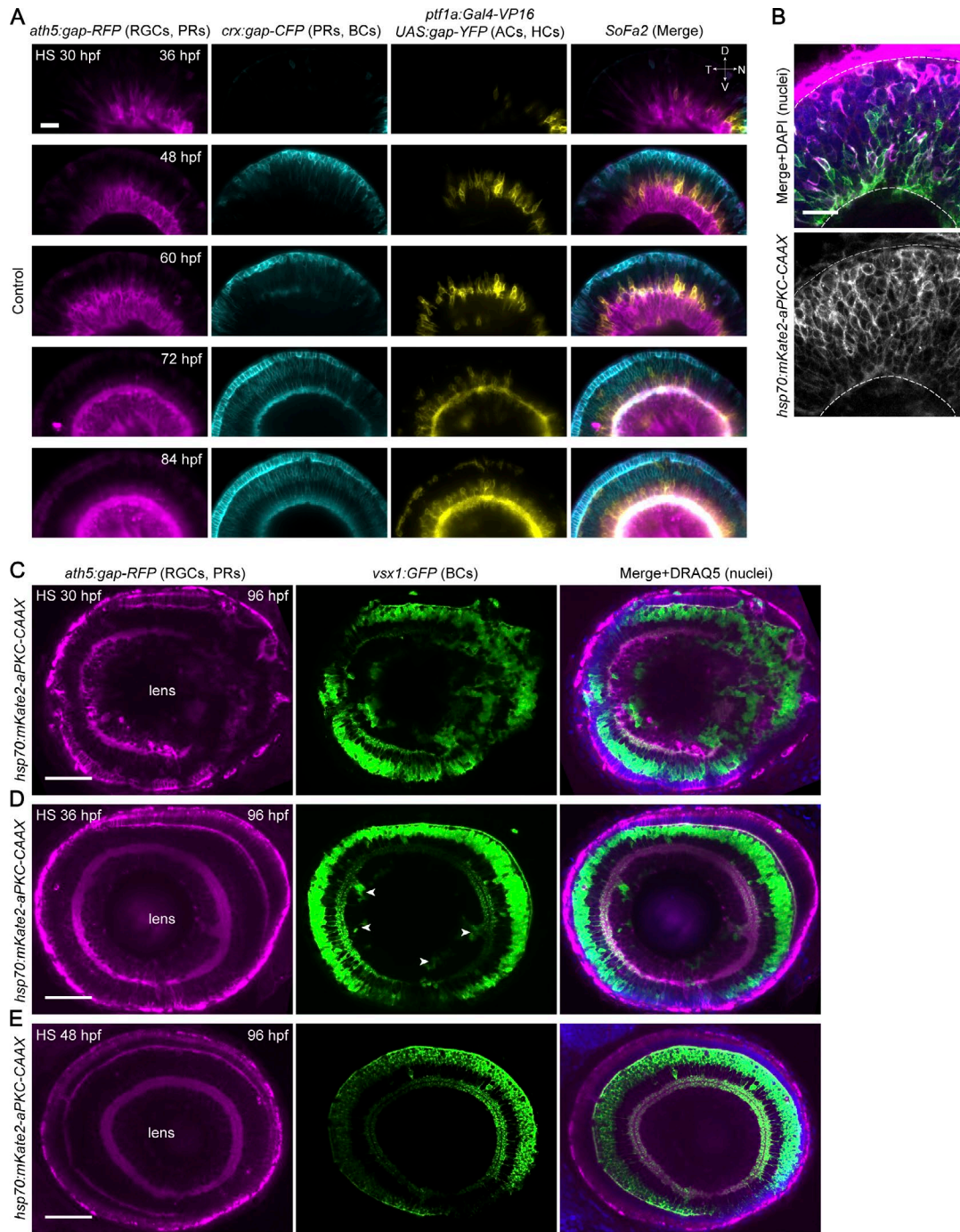
Figure S5. **The effect of aPKC-CAAX overexpression on retinal lamination and related control experiments.** (A) Control retina development. The *SoFa2* transgenic fish (combination of *ath5:gap-RFP* [labeling RGCs and photoreceptors (PRs)], *crx:gap-CFP* [labeling photoreceptors and bipolar cells (BCs)], *ptf1a:Gal4-VP16 UAS:gap-YFP* [labeling horizontal cells (HCs) and ACs]) were heat shocked (HS) at 32 hpf and imaged in the LSFM from 36 hpf every 12 h. The fish were kept in the incubator between the time points. No ectopic RGCs developed. (B) Fluorescence signal of the *hsp70:mKate2-aPKC-CAAX* construct from Fig. 6 C. Fish were heat shocked at 30 hpf, fixed at 48 hpf, and stained with Zn5 antibody. The fluorescence of mKate2-aPKC-CAAX is only detectable within 24 h of heat shock because of the fast turnover of the protein. The dashed lines mark the apical and basal membranes of the retina. (A and B) Bars, 20 µm. (C–E) aPKC-CAAX perturbs retinal lamination only during a short time window. The *ath5:gap-RFP, vsx1:GFP, hsp70:mKate2-aPKC -CAAX* triple transgenic line was heat shocked at 30 (C), 36 (D), or 48 hpf (E), fixed at 96 hpf, and stained with DRAQ5 to additionally label the nuclei. The severe lamination problems can be observed in C. Mild phenotype can be seen in D with only a few ectopic clusters of bipolar cells (arrowheads), and in E, the retina is indistinguishable from the control (Fig. 7 A) with only one continuous RGC layer and the whole retina forming an unperturbed layered structure. Bars, 50 µm.
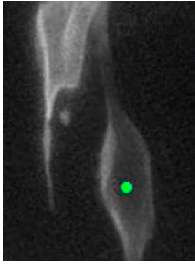
Video 1. **Somal translocation and basal process inheritance of RGCs and progenitors.** (Part 1) Typical example of RGC translocation in LSFM, when RGC inherits the basal process. Membranes of RGCs are labeled by *ath5:gap-RFP* (gray). Time is shown in hours and minutes. Green dot, RGC during directional phase; gray dot, RGC during fine positioning phase; arrowheads, inherited basal process. (Part 2) The RGC not inheriting the basal process. Membranes of RGCs are labeled by *ath5:GFP-CAAX* (gray). Blue arrow, axon. (Part 3) Inheritance of basal process in progenitors. Membranes of cells are labeled by *bactin:mKate2 -ras* (gray), and nuclei are labeled by *hsp70:GFP-PCNA* (green). White dot, basal process inheriting progenitor; arrowheads, inherited basal process; arrows, newly formed basal process of the sister cell.
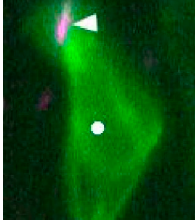

Video 2. **Organelle positions during RGC translocation.** (Part 1) Centrosome position during RGC translocation. The centrosome is labeled with *centrin-tdTomato* (magenta, white arrowhead). Membrane of RGC (white dot) is labeled by *ath5:GFP-CAAX* (green). Time is shown in hours and minutes. (Part 2) The primary cilium is labeled with *hsp70:Arl13b-mKate2* (magenta, white arrowhead). The membrane of RGC (white dot) is labeled by *ath5:GFP-CAAX* (green), and the axon is labeled by the blue arrow. (Part 3) Golgi apparatus position during RGC translocation. Golgi is labeled with *hsp70:GalT-RFP* (magenta, white arrowhead). Membrane of RGC (white dot) is labeled by *ath5:GFP-CAAX* (green).
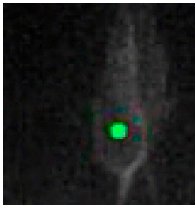

Video 3. **Live imaging of RGC translocation after ROCK inhibition.** 100 µM Rockout was added at the start of imaging. Note that RGC loses the basal process but keeps the apical process. Membranes of RGCs (green dot) are labeled by *ath5:gap-RFP* (gray). Time is shown in hours and minutes.
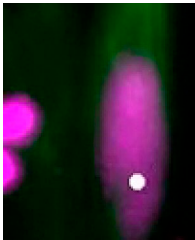
Video 4. **Live imaging of MTs in translocating RGCs.** MTs are labeled by *ath5:GFP-DCX* (green) and nuclei by *ath5 :H2B-RFP* (magenta). Note MT accumulation in the apical process. Time is shown in hours and minutes. White dot, RGC followed; blue arrow, axon.
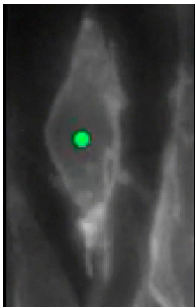
Video 5. **Multipolar migratory mode.** (Part 1) Multipolar migration in wild type. Time is shown in hours and minutes. Green dot, RGC followed. (Part 2) Multipolar migration induced by MT destabilization. Stathmin 1 (magenta) overexpression was induced at 30 hpf. Video starts at 34 hpf. Note higher protrusive activity upon loss of the basal and apical processes. White dot, RGC followed; blue arrow, axon. (Part 3) Multipolar migration induced by Arp2/3 inhibition. NWASP-CA (magenta) overexpression induced at 30 hpf. Video starts at 34 hpf. White dot, RGC followed. (Part 4) AC translocation. *bactin:ras-GFP* (green), *ptf1a :dsRed* (magenta) double transgenic embryos were used as donors for blastomere transplantation into wild-type acceptors. The translocating AC (white dot) initially has the apical process, and its loss triggers faster directional movement to the final position.
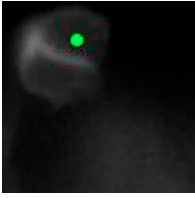
Video 6. **No RGC translocation upon aPKC-CAAX overexpression.** (Part 1) No RGC translocation upon aPKC-CAAX overexpression. Membrane of RGC is labeled by *ath5:GFP-CAAX* (gray). Time is shown in hours and minutes. Green dot, RGC followed; blue arrow, axon. (Part 2) Impaired RGC translocation upon *ath5:aPKC-CAAX* (magenta) expression. Membrane of RGC is labeled by *ath5:GFP-CAAX* (green). White dot, RGC followed; blue arrow, axon.

A script for detection of apoptotic cells is also available as a Word file.